


Cite this: *Energy Adv.*, 2025,  
4, 1251

# First principles study of alkali metal-decorated bismuth selenide for hydrogen storage applications

Asma Kiran,<sup>a</sup> Saleh S. Alarfaji,<sup>bc</sup> Muhammad Bilal Tahir<sup>d</sup> and  
Muhammad Isa Khan <sup>\*a</sup>

The identification of novel two-dimensional materials is often highly valued because of their extraordinary characteristics and prospective uses. This study presents a new bismuth selenide ( $\text{Bi}_2\text{Se}_3$ ) monolayer based on density functional theory (DFT). Its bandgap, state density, and mobilities are determined and examined. This study investigates hydrogen storage in  $\text{Bi}_2\text{Se}_3$  adorned with alkali metal (Li/Na and K) atoms. The optimal adsorption site for alkali metal (AM) atoms on the  $\text{Bi}_2\text{Se}_3$  monolayer is located above an Se atom. The AM atoms are physically adsorbed on  $\text{Bi}_2\text{Se}_3$ , and the electronic charge shifts from these to the  $\text{Bi}_2\text{Se}_3$  monolayer. In all scenarios examined, hydrogen molecules are physically adsorbed onto AM- $\text{Bi}_2\text{Se}_3$  complexes, suggesting that these systems could be employed for hydrogen storage. The K- $\text{Bi}_2\text{Se}_3$  monolayer shows the highest hydrogen storage capacity, with one potassium atom adsorbing up to 19 hydrogen molecules, while both Na- $\text{Bi}_2\text{Se}_3$  and Li- $\text{Bi}_2\text{Se}_3$  could adsorb 18 hydrogen molecules. It is estimated that the hydrogen-storage gravimetric capacities of AM- $\text{Bi}_2\text{Se}_3$  are within the US-DOE criteria, where the adatom coverage reaches about 6.71 wt% for K, 6.52 wt% for Na, and 6.66 wt% for Li.

Received 30th May 2025,  
Accepted 12th August 2025

DOI: 10.1039/d5ya00149h

rsc.li/energy-advances

## 1 Introduction

Energy crisis is a significant concern for humanity. Particularly in the aftermath of the epidemic, the global scenario is experiencing profound transformations that could directly or indirectly affect the energy market, potentially leading to risks in global energy collaboration.<sup>1</sup> Moreover, mankind's requirement for energy has increased, exacerbating the depletion of conventional fossil energy sources.<sup>2,3</sup> Conventional high-pressure and cryogenic liquid hydrogen storage methods are expensive, inconvenient to transport, and pose explosion risks.<sup>4</sup> Therefore, scientists have concentrated on solid-state hydrogen storage owing to its large capacity, better safety, and efficient hydrogen uptake and discharge processes.<sup>5–7</sup>

The use of 2D materials for physical adsorption in hydrogen storage has attracted significant attention as an emerging technology. Powerful hydrogen storage entails the adsorption

of  $\text{H}_2$  molecules on the surface of a 2D material *via* intermolecular forces.<sup>7</sup> A material used for productive hydrogen storage must satisfy the criteria of energy and weight density. The  $\text{H}_2$  adsorption energy on the substrate must range from  $-0.20$  to  $-0.70$  eV to promote integration/extraction processes under optimal operational conditions.<sup>8–10</sup> Moreover, the gravimetric density of  $\text{H}_2$  should reach a minimum of 6.5% by weight, following the measures established by the U.S. DOE. More recently, scientists have explored the potential of 2D materials as ideal choices for hydrogen storage.<sup>11,12</sup> 2D materials have extensive surface regions, remarkable thermal resilience, exceptional conductivity, and resilience and are a preferred choice over alternative options. Various 2D materials have been applied in gas sensing,<sup>13,14</sup> lithium-ion batteries,<sup>14</sup> and hydrogen storage.<sup>15</sup>

The reversible  $\text{H}_2$  storage system necessitates optimal binding of  $\text{H}_2$  that is neither too strong nor too weak but falls in the physisorption range of  $0.20$ – $0.60$  eV per  $\text{H}_2$ .<sup>16</sup> Metal atoms, such as alkali metals, alkaline earth metals, and transition metals, are used to modify 2D materials to enhance their  $\text{H}_2$  storage capacity.<sup>17–23</sup> The enhanced hydrogen storage performance of boron hydride monolayers functionalized with light metal atoms has been demonstrated through theoretical investigations. Introducing structural defects into the boron hydride monolayer leads to metallization, which significantly increases its hydrogen adsorption capacity. These defect-engineered metal-

<sup>a</sup> Department of Physics, Rahim Yar Khan Campus, Islamia University of Bahawalpur, Bahawalpur, Pakistan. E-mail: asmakiran503@gmail.com, muhammad.isa@iub.edu.pk

<sup>b</sup> Department of Chemistry, Faculty of Science, King Khalid University, Abha 61413 P.O. Box 9004, Saudi Arabia. E-mail: ssalarvagi@kku.edu.sa

<sup>c</sup> Research Center for Advanced Materials Science (RCAMS), King Khalid University, P.O. Box 9004, Abha 61413, Saudi Arabia

<sup>d</sup> Institute of Physics, Khwaja Fareed University of Engineering and Information Technology, Rahim Yar Khan, Pakistan. E-mail: m.bilaltahir@kfueit.edu.pk

dispersed boron hydride systems represent promising platforms for high-efficiency hydrogen storage applications, offering improved binding energies and reversible adsorption characteristics suitable for next-generation energy technologies.<sup>24,25</sup>

Motivated by the recent successful synthesis of the Dirac material BeN<sub>4</sub>, Mahamiya *et al.* explored the interaction of dihydrogen molecules with both pristine and scandium-functionalized BeN<sub>4</sub> monolayers using dispersion-corrected density functional theory (DFT) and *ab initio* molecular dynamics simulations. This study demonstrates that the adsorption strength of hydrogen can be significantly enhanced by metal atom decoration. Scandium, the lightest transition metal with the highest number of unoccupied d-orbitals in the 3d series, exhibits a strong affinity for hydrogen *via* Kubas interactions, enabling it to accommodate multiple hydrogen molecules. Consequently, Sc atoms were introduced onto the BeN<sub>4</sub> surface to enhance hydrogen binding energy and increase the desorption temperature, thereby improving the material's potential for efficient hydrogen storage.<sup>26</sup> Panigrahi *et al.* employed first-principles density functional theory (DFT) calculations to investigate the potential of BCN monolayers as effective hydrogen (H<sub>2</sub>) storage materials. The inclusion of van der Waals corrections revealed that light metal dopants, such as Li, Na, K, Mg, and Ca, exhibit strong binding affinities to defective BCN, with binding energies of −3.41, −2.52, −2.93, −2.27, and −4.24 eV, respectively. These substantial binding energies effectively suppress the tendency of metal atoms to aggregate on the BCN surface, promoting uniform dispersion.<sup>27</sup>

Lithium enhances hydrogen adsorption on 2D material surfaces and significantly increases the gravimetric hydrogen storage density.<sup>28–30</sup> In 2016, Das *et al.* investigated hydrogen storage by replacing one hydrogen atom with lithium on both the boron and nitrogen sides of a hydrogenated hexagonal boron nitride sheet.<sup>31</sup> Solimannejad *et al.* discovered that a Li-decorated double-sided B<sub>2</sub>N<sub>2</sub> nanosheet can adsorb 8 H<sub>2</sub> molecules, reaching a storage capacity of 12.4 wt% with dehydrogenation possible at 288 K and 1 atm.<sup>32</sup> In 2022, Yong *et al.* studied H<sub>2</sub> adsorption on Ca-decorated graphitic nanoporous CN monolayers, finding an average adsorption energy of −0.16 to −0.23 eV and a storage capacity of 10.1 wt%.<sup>33</sup> In 2023, Zhang *et al.* reported that double-sided Li-decorated 2D Iridagraphene adsorbed 24 H<sub>2</sub> molecules with an adsorption energy of −0.27 eV per H<sub>2</sub> and a storage density of 7.1 wt%.<sup>34</sup> All these substances exhibit exceptional hydrogen storage performance.

For over five decades, A<sub>2</sub>B<sub>3</sub> compounds, where A represents Bi and Sb, and B denotes Se and Te, have been renowned for their outstanding thermoelectric characteristics.<sup>35–37</sup> Bi<sub>2</sub>Se<sub>3</sub> is a good thermoelectric material owing to its exceptional thermoelectric performance and distinctive electronic structure proximate to the band gap. Bi<sub>2</sub>Se<sub>3</sub> exhibits potential applications for cooling at room temperature.<sup>38</sup> Bi<sub>2</sub>Se<sub>3</sub> plays a crucial role in environmentally efficient solid-state cooling systems. These systems efficiently convert waste heat into electrical energy and are likewise suitable for optoelectronic technologies. They are used in the manufacturing of devices for various purposes, including heat regeneration and moisture detection,<sup>39</sup> solid-phase thermoelectric

power sources,<sup>40</sup> emission detectors,<sup>41</sup> transistors utilizing band-to-band tunneling,<sup>42</sup> and magneto electronic and photoelectrochemical devices.<sup>43</sup> In recent studies, scientists have identified topological insulator behavior in Bi<sub>2</sub>Se<sub>3</sub>, Bi<sub>2</sub>Te<sub>3</sub>, and Sb<sub>2</sub>Te<sub>3</sub>. Certain experimental procedures are used to prepare 2D A<sub>2</sub>B<sub>3</sub> structures. As an illustration, Kong *et al.*<sup>44</sup> achieved ultrathin nanoplates of Bi<sub>2</sub>Te<sub>3</sub> and Bi<sub>2</sub>Se<sub>3</sub> consisting of three quintuple layers through vapor–solid growth, eliminating the need for a catalyst. Liu *et al.*<sup>45</sup> synthesized Bi<sub>2</sub>Se<sub>3</sub> nanobelts using van der Waals epitaxy without catalysts and used these nanobelts to manufacture a near-infrared photodetector. Buha *et al.*<sup>46</sup> investigated the thermal robustness and anisotropic vaporization of nanocrystals made from Bismuth telluride (Bi<sub>2</sub>Te<sub>3</sub>) and Bi<sub>2</sub>Se<sub>3</sub> using localized transmission electron microscopy. Utilizing a fast resolution-based technique, Min *et al.*<sup>47</sup> successfully produced ultra-thin monocrystalline nanodiscs and nanosheets of Bi<sub>2</sub>Se<sub>3</sub>. In 2018, Wang *et al.*<sup>48</sup> conducted a theoretical investigation of the monolayer structures of Bi<sub>2</sub>Te<sub>2</sub>S and Bi<sub>2</sub>Te<sub>2</sub>Se, revealing their high electron conductivities. Lu *et al.*<sup>49</sup> discovered that the Bi<sub>2</sub>TeSe<sub>2</sub> monolayer behaves as a direct semiconductor and that strain engineering can produce exceptionally high electron mobility for the monolayer.

Our research focuses on the first principles study of alkali metal-decorated Bi<sub>2</sub>Se<sub>3</sub> for hydrogen storage applications. DFT was utilized to explore the interaction mechanisms between hydrogen and Bi<sub>2</sub>Se<sub>3</sub> when decorated with alkali metals. This approach provides insights into the potential of these materials for efficient and sustainable hydrogen storage and offers a promising alternative to conventional energy sources.

## 2 Computational details

All computations related to the investigation of alkali metal (Li/Na/K) modification of Bi<sub>2</sub>Se<sub>3</sub> for hydrogen storage purposes, including energetic equilibrium and configurations, were conducted using the Amsterdam density functional (ADF) module BAND within the context of DFT.<sup>50</sup> Slater-type orbitals integrated into the ADF-BAND calculations were employed to compute the molecular orbitals of each structure. Throughout this study, double-zeta polarized (DZP) sets, characterized by regular numerical precision and a core-electron treatment method, were consistently utilized.<sup>51</sup> GGA (generalized gradient approximation) within the PBE approximation method was used to calculate the correlation–exchange interactions among electron particles.<sup>52</sup>

The numerical accuracy of ADF hinges on the *k*-grid, basis set, and variables in density fitting as fundamental components. These particular *k*-points effectively represent a sampling of the Brillouin Zone and incorporate a fuzzy partition scheme pioneered and established by Becke.<sup>53</sup> Corrections to van der Waals effects were also included to ensure the relaxation of all configurations to their optimal equilibrium structure, employing the observational Grimme dispersion technique.<sup>54</sup> For the relaxation of all structures, the criteria for the convergence of energy, gradient, and step were defined as 10<sup>−5</sup> eV, 0.02 eV Å<sup>−1</sup>, and



$10^{-3}$  Å, respectively. In our previous study, we utilized computational methods to devise and elucidate the structural and electronic characteristics of  $\text{Bi}_2\text{Se}_3$ . Furthermore, detailed discussions were conducted on the configurations, adsorption locations, and state density resulting from attachment involving alkali metal (Li/Na/K) atoms upon  $\text{Bi}_2\text{Se}_3$ .<sup>55</sup> The adsorption energy for  $\text{Bi}_2\text{Se}_3$  can be determined using the following formula:

$$E_{\text{ads}} = [E_{\text{Bi}_2\text{Se}_3+\text{A.M}} + nE_{\text{H}_2} - E_{\text{Bi}_2\text{Se}_3+\text{A.M}+n\text{H}_2}]/n, \quad (1)$$

where  $E_{\text{Bi}_2\text{Se}_3+\text{A.M}}$  represents the total energy of  $\text{Bi}_2\text{Se}_3$  about alkali metals (Li/Na/K),  $E_{\text{Bi}_2\text{Se}_3+\text{A.M}+n\text{H}_2}$  denotes the total energy of  $\text{Bi}_2\text{Se}_3$  adorned with alkali metals (Li/Na/K),  $n$  denotes the number of hydrogen molecules and  $E_{\text{H}_2}$  denotes the energy of a lone hydrogen molecule.<sup>56,57</sup>

van der Waals long-range dispersion correction in ADF: BAND was utilized in all computations owing to its advantageous impact on improving adsorption energy.<sup>57</sup>

Binding energy might be determined using the following equation:

$$E_{\text{B}} = E_{\text{Bi}_2\text{Se}_3+\text{A.M}} - E_{\text{Bi}_2\text{Se}_3} - E_{\text{A.M}}, \quad (2)$$

where  $E_{\text{Bi}_2\text{Se}_3}$  represents the energy of unaltered  $\text{Bi}_2\text{Se}_3$ ,  $E_{\text{A.M}}$  denotes the energy of a solitary alkali metal atom (Li/Na/K) with varying counts of  $n = (1, 2, 3, 4, 5)$ , and  $E_{\text{Bi}_2\text{Se}_3+\text{A.M}}$  denotes the combined total energy of  $\text{Bi}_2\text{Se}_3$  decorated with A.M (Li/Na/K) atoms.<sup>57,58</sup>

We determined the  $\text{H}_2$  temperature desorption by applying the following van't Hoff's equation:<sup>59</sup>

$$T_{\text{d}} = \frac{E_{\text{ads}}}{K_{\text{B}}} \left( \frac{\Delta S}{R} - \ln p \right)^{-1}, \quad (3)$$

where the Boltzmann constant  $K_{\text{B}}$  equals  $1.38 \times 10^{-23} \text{ J K}^{-1}$ , the variation in entropy is  $\Delta S$ , the transition from hydrogen converting from gas to liquid involved is  $75.44 \text{ J mol}^{-1} \text{ K}^{-1}$ , and the gas constant ( $R$ ) for  $\text{H}_2$  is  $8.314 \text{ J mol}^{-1} \text{ K}^{-1}$ , with an equilibrium pressure ( $p$ ) of 1 atm.<sup>56</sup> First-principles molecular dynamics (MD) simulations were conducted to confirm the structural stability of the substrate at both ambient and desorption temperatures.

The calculation involved determining the gravimetric storage capacity (GC).<sup>60</sup>

$$G_{\text{c}}(\text{wt}\%) = \frac{n_{\text{H}_2} \times W_{\text{H}_2}}{n_{\text{Bi}} \times W_{\text{Bi}} + n_{\text{Se}} \times W_{\text{Se}} + n_{\text{A.M}} \times W_{\text{A.M}} + n_{\text{H}_2} \times W_{\text{H}_2}} \times 100\%, \quad (4)$$

where  $n_{\text{H}_2}$ ,  $n_{\text{Bi}}$ ,  $n_{\text{Se}}$  and  $n_{\text{A.M}}$  represent the quantities of  $\text{H}_2$  molecules and Bi, Se, and A.M atoms, respectively, while  $w_{\text{H}_2}$ ,  $w_{\text{Bi}}$ ,  $w_{\text{Se}}$  and  $w_{\text{A.M}}$  denotes the weights of  $\text{H}_2$  molecules and Bi, Se, and A.M atoms, respectively.

## 3 Results and discussion

### 3.1 Structural and electronic properties of $\text{Bi}_2\text{Se}_3$

Fig. 1(a) presents the optimized structure of  $\text{Bi}_2\text{Se}_3$ , which is shown from both the  $z$ -axis and  $x$ -axis perspectives. It consists of bismuth (Bi) and selenium (Se) atoms. It is categorized within

the group of materials referred to as topological insulators.  $\text{Bi}_2\text{Se}_3$  is a compound with notable structural properties that make it suitable for various applications, including electronic and thermoelectric devices. It is famous owing to its distinctive layer structure. Each quintuple layer consists of five atomic layers arranged in a specific sequence: Se–Bi–Se–Bi–Se. These quintuple layers are weakly bonded to each other by van der Waals forces, allowing for easy cleavage along the layers. The Bi atoms are bonded with Se atoms in a trigonal planar arrangement. The lattice parameters for the  $\text{Bi}_2\text{Se}_3$  hexagonal crystal structure are  $a = 4.137$  Å and  $c = 28.64$  Å. The bonding within the quintuple layers is covalent, while the interaction between the layers is primarily van der Waals. This material has already been studied for topological insulators and spintronics. The distances between bismuth and selenium atoms in  $\text{Bi}_2\text{Se}_3$  range from 2.86 Å to 3.10 Å. The angles formed between adjacent atoms in the crystal structure are in the range of  $46^\circ$ – $91^\circ$ .

The phonon dispersion is shown in Fig. 1(d), and the results are consistent with the study. According to Zhan *et al.*,<sup>61</sup> phonon dispersion confirms the stability of the monolayer. Imaginary frequency is absent within the first reciprocal lattice cell, indicating dynamic durability of the  $\text{Bi}_2\text{Se}_3$  monolayer. The electronic properties are derived from the optimized geometric structure of  $\text{Bi}_2\text{Se}_3$  single layers. The  $\text{Bi}_2\text{Se}_3$  monolayer exhibits a 0.75 eV indirect energy bandgap, as illustrated in Fig. 1(b) and (c). Detailed examination of atomic components in the density of states (DOS) is shown in Fig. 1(b). It is evident that the conduction band minimum (CBM) of the  $\text{Bi}_2\text{Se}_3$  single atomic layer is primarily composed of p orbitals associated with Bi, with a small impact from the p orbitals of the Se atoms. However, the valence band maximum (VBM) is observed to be composed solely of p orbitals of Se atoms, with no significant charge distribution on the Bi atoms.

### 3.3 Adsorption of hydrogen on pristine $\text{Bi}_2\text{Se}_3$

Here, we examined the interaction of a solitary  $\text{H}_2$  molecule characterized by an unmodified  $\text{Bi}_2\text{Se}_3$  interface. Three distinct adsorption sites, namely (i) Se, (ii) Bi, and (iii) bridge within the  $\text{Bi}_2\text{Se}_3$  structure, were selected for investigation. We explored the associated binding energies for these potential sites, considering both with and without London dispersion forces. The illustration depicts hydrogen binding on an unmodified  $\text{Bi}_2\text{Se}_3$  surface. Subsequently, we delve into the stability characteristics of pure  $\text{Bi}_2\text{Se}_3$  upon hydrogen adsorption. The geometric distances between the adsorption site and the  $\text{H}_2$  molecules vary, ranging from the Bi site (5.09–5.85 Å) to the Se site (2.90–3.82 Å). The horizontal alignment with Bi and Se involves an  $\text{H}_2$  molecule at each of two potential binding positions to compute the interaction energy. It is clear that the  $\text{H}_2$  molecule has maintained its bonding and bond length of 0.75 Å and has not split into two distinct H atoms.<sup>44</sup>

The binding energy of the  $\text{H}_2$  molecule over pure  $\text{Bi}_2\text{Se}_3$  can be calculated as follows:<sup>62</sup>

$$E_{\text{b}} = \frac{E_{\text{Bi}_2\text{Se}_3+n\text{H}_2} - E_{\text{Bi}_2\text{Se}_3} - E_{n\text{H}_2}}{n} \quad (5)$$

where  $E_{\text{Bi}_2\text{Se}_3+n\text{H}_2}$ ,  $E_{\text{Bi}_2\text{Se}_3}$  and  $E_{n\text{H}_2}$  represent the energy of



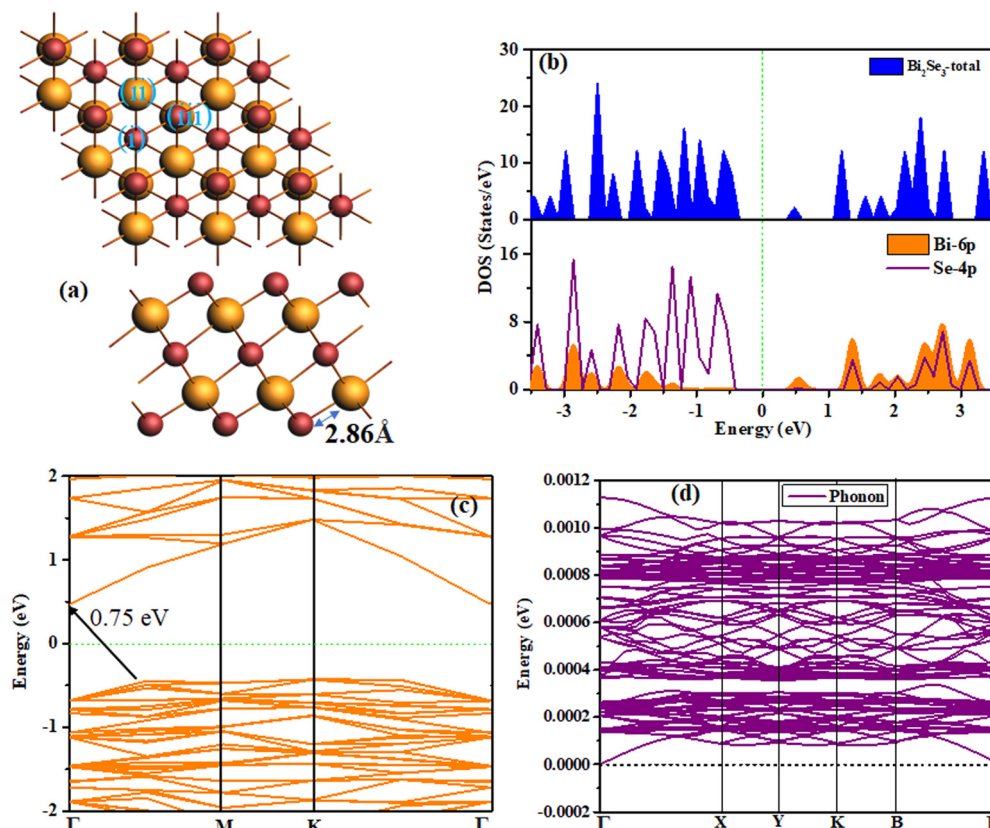


Fig. 1 (a) Z and X-views of the optimized structure of pure Bi<sub>2</sub>Se<sub>3</sub>, (b) Partial density of states (PDOS), (c) band structure, and (d) phonon dispersion curves.

Table 1 Binding energies (in eV per H<sub>2</sub>) of H<sub>2</sub> on pristine Bi<sub>2</sub>Se<sub>3</sub> at various locations

Adsorption site	Se	Bi	Bridge
$E_b$ (eV)	−0.18	−0.17	−0.19

adsorption of hydrogen on Bi<sub>2</sub>Se<sub>3</sub>, the energy of pure Bi<sub>2</sub>Se<sub>3</sub>, and the energy of the hydrogen molecule, respectively. The binding energies are listed in Table 1.

This indicates which H<sub>2</sub> molecules could interact with Bi<sub>2</sub>Se<sub>3</sub> via London dispersion forces. This sequence of molecular adsorption energies indicates pristine Bi<sub>2</sub>Se<sub>3</sub>.<sup>60</sup>

The calculated results indicate that the Br site exhibits the highest adsorption energy, identifying it as the most favorable site for H<sub>2</sub> adsorption in the pristine Bi<sub>2</sub>Se<sub>3</sub> monolayer. However, although adsorption occurs successfully, the corresponding energy values do not meet the benchmark established by the U.S. Department of Energy (US-DOE) for efficient hydrogen storage. To address this limitation and enhance the binding energy within the DOE-specified range, alkali metal decoration is proposed as a strategy to improve hydrogen storage performance.

### 3.3 Adsorption and electronic properties of AM on Bi<sub>2</sub>Se<sub>3</sub>

Initially, the investigation focused on the interaction between Li/Na/K atoms and the Bi<sub>2</sub>Se<sub>3</sub> monolayer. With this consideration in mind, lightweight alkali metals were adsorbed onto

Bi<sub>2</sub>Se<sub>3</sub>. By exploring various adsorption sites on the Bi<sub>2</sub>Se<sub>3</sub> base, we identified the optimal adsorption site for a lone Li/Na/K atom in the monolayer. The adsorption characteristics concerning a single Li, Na, or K atom at three different sites (Bi, Se, and Br) on the Bi<sub>2</sub>Se<sub>3</sub> surface were calculated, as illustrated in Fig. 2. Metal tends to create stable compounds above the Se atom of Bi<sub>2</sub>Se<sub>3</sub>. The energetic stability of metal-decorated Bi<sub>2</sub>Se<sub>3</sub> was explored by investigating the binding energy using eqn (2).

The binding energy for each metal species in Li/Na/K-Bi<sub>2</sub>Se<sub>3</sub> is measured to be −1.72 eV, −1.44 eV, and −1.99 eV, respectively. The feasibility of metal adherence as a process is indicated by the negative values of  $E_b$  per metal adsorbent. The binding energy ( $E_b$ ) of Li at Bi<sub>2</sub>Se<sub>3</sub> is observed to be greater than its cohesive energy in bulk, which is 1.63 eV.<sup>63</sup> Likewise, binding energy ( $E_b$ ) values for Na-Bi<sub>2</sub>Se<sub>3</sub> and K-Bi<sub>2</sub>Se<sub>3</sub> complexes are also greater than those of bulk metals, where Na exhibits a cohesive energy of −1.13 eV and bulk K exhibits a cohesive energy of −0.93 eV. Higher binding energy ( $E_b$ ) values for metal adsorbents Li, Na, and K, compared to their respective lattice energies, suggest that metal collection is unlikely within the system. After adsorption, the Bi<sub>2</sub>Se<sub>3</sub> monolayer shows a Se-Li bond distance of 2.54 Å, while the Bi-Li distance is 3.58 Å. The Se-Na bond distance in the Bi<sub>2</sub>Se<sub>3</sub> monolayer is 2.89 Å, while the Bi-Na distance is 4.05 Å. In the Bi<sub>2</sub>Se<sub>3</sub> monolayer following adsorption, the Se-K bond distance is 3.23 Å, while the distance between Bi and K is 4.46 Å.





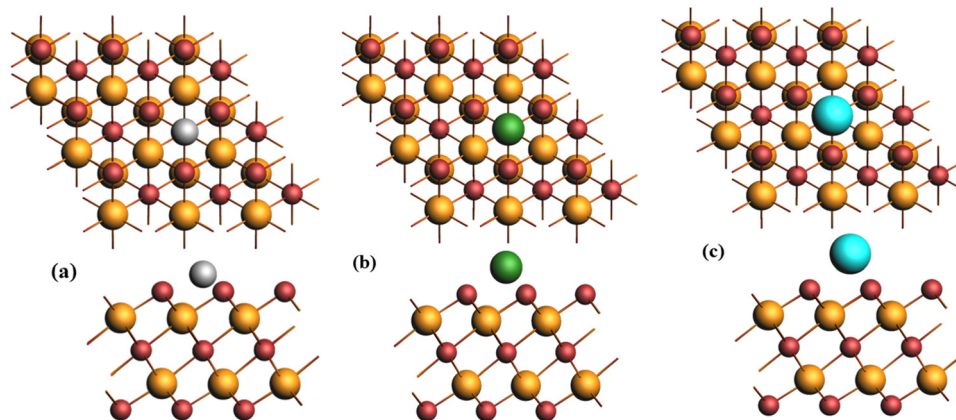


Fig. 2 Views of optimized configurations of (a) Li-, (b) Na- and (c) K-modified  $\text{Bi}_2\text{Se}_3$ .

The DOS plot illustrates the distribution of electron energy levels across different materials. The  $x$ -axis represents energy, while the  $y$ -axis indicates the number of available energy states at each energy level. Peaks in the plot highlight energy ranges with a high density of electron states. In DOS plots Fig. 3(a)–(c), the contributions of Li-2s/2p, Na-2s/2p, and K-2s/2p states are displayed. For each alkali metal, the distribution of states near the Fermi level sheds light on their interaction with adsorbed hydrogen. Peaks near  $-5$  eV correspond to the 2s states, and those around  $-3$  eV correspond to the 2p states. Moving from Li to K, the peaks shift to lower energies, indicating the decreasing ionization energy of these metals. Lithium exhibits moderate states near the Fermi level, implying weaker bonding and lower desorption energy, which makes hydrogen easily released. Sodium shows broader peaks near the Fermi level, indicating stronger adsorption with hydrogen, while potassium displays even stronger interaction, as observed from larger peaks, leading to higher desorption energy and more difficult hydrogen release.

In lower panel Fig. 3(d)–(f), the DOS of the combined system, including the substrate atoms (likely  $\text{Bi}_2\text{Se}_3$ , with Bi-6p and Se-4p orbitals), is presented along with the alkali metals. Peaks of around  $-15$  eV and  $-10$  eV for Bi and Se correspond to their 6p and 4p states, respectively. The composite material features peaks associated with the 2s and 2p states of Li, Na, and K, as well as the 6p and 4p states of Bi and Se. Overlapping peaks indicate hybridization between the states of different elements, leading to the formation of new energy bands in the composite material. K shows stronger hybridization compared to Li and Na, correlating with its higher desorption energy.

### 3.4 Adsorption and desorption of $\text{H}_2$ molecules on AM-decorated $\text{Bi}_2\text{Se}_3$

The adsorption behavior relating to hydrogen on Li, Na, and K metal-decorated  $\text{Bi}_2\text{Se}_3$  was further examined, as shown in

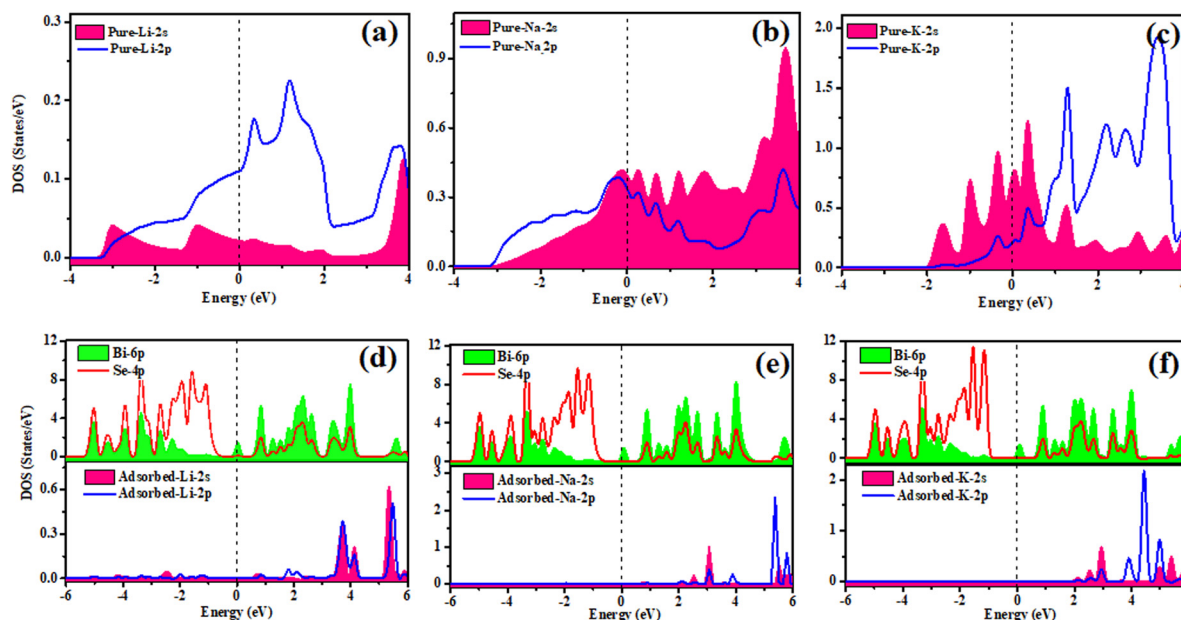


Fig. 3 Projected density of states (PDOS) for unbound (a) pure Li, (b) Na, and (c) K and adsorbed (d)  $\text{Bi}_2\text{Se}_3$ -Li, (e)  $\text{Bi}_2\text{Se}_3$ -Na, and (f)  $\text{Bi}_2\text{Se}_3$ -K.



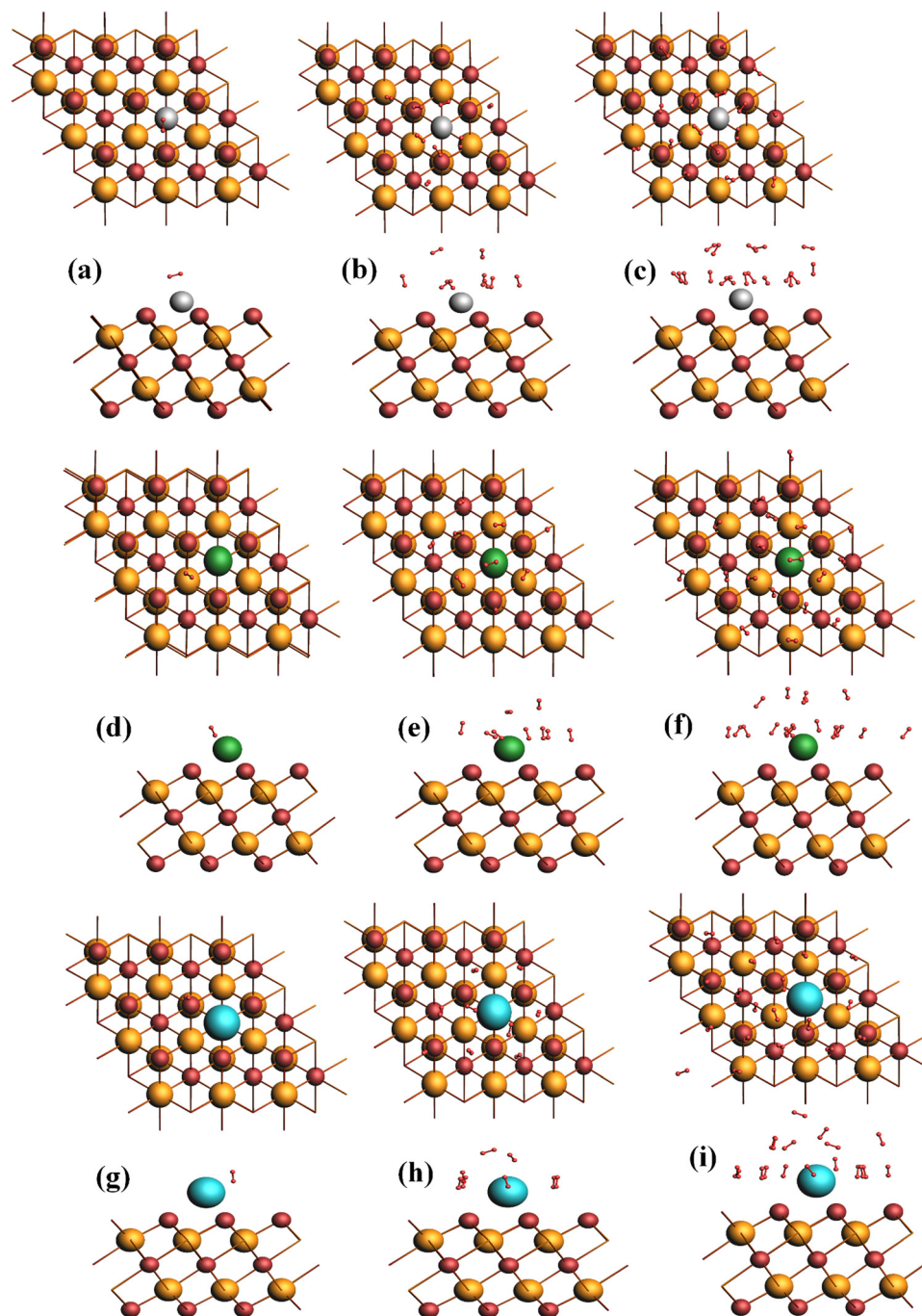


Fig. 4 Optimized geometry of Li-Bi<sub>2</sub>Se<sub>3</sub>: (a) 1H<sub>2</sub>, (b) 9H<sub>2</sub>, (c) 18H<sub>2</sub>, Na-Bi<sub>2</sub>Se<sub>3</sub>, (d) 1H<sub>2</sub>, (e) 9H<sub>2</sub>, (f) 18H<sub>2</sub>, K-Bi<sub>2</sub>Se<sub>3</sub>, (g) 1H<sub>2</sub>, (h) 9H<sub>2</sub> and (i) 19H<sub>2</sub>.

Fig. 4 (*z* and *x*-axis views). Initially, an isolated hydrogen molecule was introduced into the system, and it was observed that the hydrogen molecule was inclined towards the metal atom on the substrate. This one-inclined orientation associated with the H<sub>2</sub> molecule increases its consistency and facilitates the adsorption of additional hydrogen molecules.<sup>64</sup> The distances between the hydrogen molecule and the active site of the metal atoms are 2.32 Å, 2.58 Å, and 3.09 Å. The bond length of the adsorbed hydrogen molecule is 0.75 Å. It remains the same as that of hydrogen molecules without adsorption. To determine the stability

of complexes formed after H<sub>2</sub> binds to the surface of Li/Na/K-Bi<sub>2</sub>Se<sub>3</sub>, adsorption energy data were computed, as detailed in Table 2. Subsequently, successive adsorption of H<sub>2</sub> on the surface of Li/Na/K-Bi<sub>2</sub>Se<sub>3</sub> was performed. The H<sub>2</sub>-adsorbed Li/Na/K-Bi<sub>2</sub>Se<sub>3</sub> complexes are denoted as Li/Na/K-Bi<sub>2</sub>Se<sub>3</sub> + *n*H<sub>2</sub>, where '*n*' represents several molecular hydrogens. We observed that Li-Bi<sub>2</sub>Se<sub>3</sub> and Na-Bi<sub>2</sub>Se<sub>3</sub> can adsorb 18 H<sub>2</sub> molecules, while K-Bi<sub>2</sub>Se<sub>3</sub> can adsorb 19 hydrogen molecules. Optimized structures Li/Na/K-Bi<sub>2</sub>Se<sub>3</sub> + *n*H<sub>2</sub> are displayed in Fig. 4. The stability of the complexes formed by the adsorption of hydrogen molecules on Li/Na/K-Bi<sub>2</sub>Se<sub>3</sub> was assessed



**Table 2** Calculated average adsorption energies ( $E_{\text{ads}}$ ), binding energies ( $E_{\text{b}}$ ), gravimetric storage capacity (wt%), and temperature desorption ( $T_{\text{D}}$ )

Atoms	No. of H <sub>2</sub> molecules	$E_{\text{ads}}$ (eV)	$E_{\text{b}}$ (eV)	wt%	$T_{\text{D}}$	$\beta$ (Å)
Li	1H <sub>2</sub>	−0.23	−1.42	0.39	294.2	2.50
	2H <sub>2</sub>	−0.53		0.79	677.9	2.78
	3H <sub>2</sub>	−0.42		1.18	537.2	2.64
	4H <sub>2</sub>	−0.35		1.57	447.6	4.26
	5H <sub>2</sub>	−0.31		1.96	396.5	2.31
	6H <sub>2</sub>	−0.27		2.34	345.3	2.26
	7H <sub>2</sub>	−0.26		2.72	332.5	2.24
	8H <sub>2</sub>	−0.25		3.09	319.7	2.21
	9H <sub>2</sub>	−0.23		3.47	294.2	2.20
	10H <sub>2</sub>	−0.22		3.84	281.4	2.21
	11H <sub>2</sub>	−0.22		4.21	281.4	2.30
	12H <sub>2</sub>	−0.21		4.57	268.6	4.12
	13H <sub>2</sub>	−0.21		4.97	268.6	2.24
	14H <sub>2</sub>	−0.20		5.30	255.8	4.06
	15H <sub>2</sub>	−0.20		5.65	255.8	4.18
	16H <sub>2</sub>	−0.20		6.01	255.8	4.26
	17H <sub>2</sub>	−0.19		6.36	243.0	4.44
	18H <sub>2</sub>	−0.19		6.66	243.0	2.18
Na	1H <sub>2</sub>	−0.20	−1.72	0.38	255.8	2.58
	2H <sub>2</sub>	−0.48		0.76	613.9	2.55
	3H <sub>2</sub>	−0.39		1.14	498.8	2.56
	4H <sub>2</sub>	−0.33		1.52	422.1	2.66
	5H <sub>2</sub>	−0.29		1.90	370.9	2.71
	6H <sub>2</sub>	−0.27		2.27	345.3	2.59
	7H <sub>2</sub>	−0.25		2.64	319.7	2.61
	8H <sub>2</sub>	−0.24		3.00	307.0	4.54
	9H <sub>2</sub>	−0.23		3.37	294.2	4.64
	10H <sub>2</sub>	−0.22		3.73	281.4	4.69
	11H <sub>2</sub>	−0.21		4.08	268.6	2.94
	12H <sub>2</sub>	−0.21		4.44	268.6	4.53
	13H <sub>2</sub>	−0.20		4.79	255.8	4.80
	14H <sub>2</sub>	−0.20		5.14	255.8	2.65
	15H <sub>2</sub>	−0.20		5.49	255.8	2.71
	16H <sub>2</sub>	−0.19		5.83	243.0	2.70
	17H <sub>2</sub>	−0.19		6.18	243.0	2.64
	18H <sub>2</sub>	−0.19		6.50	243.0	2.65
K	1H <sub>2</sub>	−0.67	−1.99	0.37	856.9	3.09
	2H <sub>2</sub>	−0.46		0.74	588.3	3.00
	3H <sub>2</sub>	−0.37		1.11	473.2	3.07
	4H <sub>2</sub>	−0.32		1.48	409.3	3.08
	5H <sub>2</sub>	−0.29		1.84	370.9	3.07
	6H <sub>2</sub>	−0.26		2.20	332.5	3.11
	7H <sub>2</sub>	−0.25		2.56	319.7	3.07
	8H <sub>2</sub>	−0.23		2.91	294.2	3.07
	9H <sub>2</sub>	−0.23		3.27	294.2	3.59
	10H <sub>2</sub>	−0.22		3.62	281.4	3.15
	11H <sub>2</sub>	−0.21		3.97	268.6	3.14
	12H <sub>2</sub>	−0.21		4.31	268.6	3.15
	13H <sub>2</sub>	−0.20		4.65	255.8	6.99
	14H <sub>2</sub>	−0.20		4.99	255.8	3.16
	15H <sub>2</sub>	−0.20		5.33	255.8	3.18
	16H <sub>2</sub>	−0.19		5.67	243.0	6.84
	17H <sub>2</sub>	−0.19		6.00	243.0	3.13
	18H <sub>2</sub>	−0.18		6.33	230.2	3.12
	19H <sub>2</sub>	−0.18		6.71	232.2	3.14

using adsorption energy, as calculated in eqn (1). The adsorption energies for Li/Na/K-Bi<sub>2</sub>Se<sub>3</sub> +  $n$ H<sub>2</sub> systems are listed in Table 2. ( $E_{\text{ads}}$ ) values imply that binding H<sub>2</sub> is significantly stronger than on pristine Bi<sub>2</sub>Se<sub>3</sub>. Moreover, as shown in Table 2, the adsorption energy values for Li, Na, and K-Bi<sub>2</sub>Se<sub>3</sub> + 2H<sub>2</sub> are approximately −0.53 eV, −0.48 eV, and −0.46 eV, respectively. These adsorption energy values fall effectively within the criteria set by DOE-US. This indicates that additional H<sub>2</sub> uptake can proceed on Li/Na/K-Bi<sub>2</sub>Se<sub>3</sub>.

**Table 3** Desorption energy of hydrogen from alkali metal-decorated Bi<sub>2</sub>Se<sub>3</sub> with hydrogen atoms

$n$ H <sub>2</sub>	Li $E_{\text{des}}$ (eV)	Na $E_{\text{des}}$ (eV)	K $E_{\text{des}}$ (eV)
1	0.23	0.20	0.67
2	0.17	0.19	0.18
3	0.21	0.20	0.19
4	0.15	0.20	0.18
5	0.12	0.14	0.17
6	0.12	0.18	0.14
7	0.17	0.14	0.15
8	0.17	0.13	0.11
9	0.13	0.15	0.19
10	0.13	0.16	0.18
11	0.16	0.15	0.16
12	0.17	0.18	0.16
13	0.13	0.15	0.17
14	0.17	0.17	0.17
15	0.15	0.15	0.11
16	0.17	0.13	0.15
17	0.14	0.14	0.14
18	0.13	0.13	0.11
19	—	—	0.14

As shown in Table 2, the ( $E_{\text{ads}}$ ) values are negative for Li/Na/K-decorated Bi<sub>2</sub>Se<sub>3</sub> +  $n$ H<sub>2</sub> complexes, indicating that hydrogen adsorption is an exothermic reaction, resulting in thermally stable complexes. As successive H<sub>2</sub> adsorptions occur, a decrease in ( $E_{\text{ads}}$ ) values is observed (Table 2). For Li- and Na-decorated Bi<sub>2</sub>Se<sub>3</sub>, gradual decreases in ( $E_{\text{ads}}$ ) values (after the second H<sub>2</sub> molecule) and for K (after the first H<sub>2</sub> molecule) are mainly attributed to repulsive behavior between H<sub>2</sub> molecules, which are influenced by positively charged metal dopants.<sup>65,66</sup> Despite a decrease in the ( $E_{\text{ads}}$ ) values with increasing numbers of H<sub>2</sub> molecules, they remain well within the DOE-US limit. Therefore, decorating Bi<sub>2</sub>Se<sub>3</sub> with alkali metals significantly improves its H<sub>2</sub> storage efficiency. These adsorption energy values show that Li/Na/K-Bi<sub>2</sub>Se<sub>3</sub> complexes are stable and could be good choices for reversible hydrogen storage because they are within the range of reversible physical adsorption, which is between −0.1 and −0.6 eV.<sup>18,66</sup> Additionally, to assess H<sub>2</sub> uptake, Li/Na/K-Bi<sub>2</sub>Se<sub>3</sub> complexes were charged with specific metal atoms. In the Li-Bi<sub>2</sub>Se<sub>3</sub> within the complex, lithium metal was effectively filled onto the surface of Bi<sub>2</sub>Se<sub>3</sub>.

The addition of hydrogen resulted in a significantly increased H<sub>2</sub> gravimetric density of 6.66 wt% for Li. Na-Bi<sub>2</sub>Se<sub>3</sub> and K-Bi<sub>2</sub>Se<sub>3</sub> complexes resulted in gravimetric hydrogen uptakes of 6.52 wt% and 6.71 wt%, respectively. This indicates that the Li/Na/K-Bi<sub>2</sub>Se<sub>3</sub> complexes can achieve hydrogen weight percentages higher than the DOE-US limit, making them highly effective H<sub>2</sub> retention materials. To facilitate this, the average adsorption/desorption energies and gravimetric H<sub>2</sub> densities are summarized and compared in Table 3. This clearly illustrates that decoration with light metals improves H<sub>2</sub> storage capacity relative to most previously examined transition metal-embedded complexes. Furthermore, the impact of interactions between bound H<sub>2</sub> and Li/Na/K-Bi<sub>2</sub>Se<sub>3</sub> complexes on their electronic properties was investigated. These findings are discussed below.

The desorption energy ( $E_{\text{des}}$ ), which is the energy required to release a hydrogen molecule from the Bi<sub>2</sub>Se<sub>3</sub> monolayer, is expressed as follows:<sup>67,68</sup>





**Table 4** Analyzing the total number of adsorbed H<sub>2</sub> (*n*), the average adsorption energy (*E*<sub>ads</sub> in eV), and the weight percentage by mass for X–Bi<sub>2</sub>Se<sub>3</sub>–*n*H<sub>2</sub> (X = Li, Na, K) systems relative to earlier reports of metal-decorated two-dimensional nanosheets

Modified structure	Binding energies with metal	H <sub>2</sub> molecule adsorption energy (eV)	Amount of adsorbed H <sub>2</sub> molecules	Adsorbed H <sub>2</sub> gravimetric density (wt%)
<b>Li@Bi<sub>2</sub>Se<sub>3</sub> (this work)</b>	<b>−1.42</b>	<b>−0.24</b>	<b>18</b>	<b>6.66</b>
<b>Na@Bi<sub>2</sub>Se<sub>3</sub> (this work)</b>	<b>−1.44</b>	<b>−0.22</b>	<b>18</b>	<b>6.52</b>
<b>K@Bi<sub>2</sub>Se<sub>3</sub> (this work)</b>	<b>−1.99</b>	<b>−0.25</b>	<b>19</b>	<b>6.71</b>
Li@C <sub>9</sub> N <sub>4</sub> <sup>65</sup>	−2.51	−0.20	6	11.9
K@C <sub>9</sub> N <sub>4</sub> <sup>65</sup>	−2.01	−0.17	7	8.1
Na@C <sub>9</sub> N <sub>4</sub> <sup>65</sup>	−2.31	−0.19	6	8.7
Li@POG <sup>69</sup>	2.42	−0.22	3	9.9
Na@POG <sup>69</sup>	2.45	−0.16	5	7.7
K@POG <sup>69</sup>	2.80	−0.15	5	6.8
Li@SnC <sup>70</sup>	2.46	−0.20	3	5.5
Na@SnC <sup>70</sup>	2.06	−0.19	5	5.5
K@SnC <sup>70</sup>	2.12	−0.18	6	5.5
Li@Borophene <sup>71</sup>	2.47	−0.36	10	9.0
Na@Borophene <sup>71</sup>	2.50	−0.34	15	6.8

$$E_{\text{des}} = E_{\text{H}_2} + E_{(n-1)\text{H}_2+\text{Metal}+\text{Bi}_2\text{Se}_3} - E_{n\text{H}_2+\text{Metal}+\text{Bi}_2\text{Se}_3}, \quad (6)$$

where *E*<sub>H<sub>2</sub></sub> denotes the energy of a standalone hydrogen molecule; *E*<sub>(*n*−1)H<sub>2</sub>+Metal+Bi<sub>2</sub>Se<sub>3</sub></sub> is the overall energy of the system with (*n* − 1) adsorbed hydrogen molecules, where *n* denotes the maximum number of hydrogen molecules that can be adsorbed on the monolayer; and *E*<sub>*n*H<sub>2</sub>+Metal+Bi<sub>2</sub>Se<sub>3</sub></sub> is the total energy of the Bi<sub>2</sub>Se<sub>3</sub> with *n* adsorbed molecules.

Table 3 presents desorption energies *E*<sub>des</sub> of hydrogen molecules (*n*H<sub>2</sub>) from Li-, Na-, and K-decorated Bi<sub>2</sub>Se<sub>3</sub>. Desorption energy represents the energy required to release adsorbed hydrogen molecules, which is a critical parameter in hydrogen storage applications because it determines how easily stored hydrogen can be released when needed. In the case of Li, the desorption energy is relatively high with the adsorption of a single hydrogen molecule (0.23 eV), but it decreases as additional hydrogen molecules are adsorbed, such as 0.12 eV for 5 H<sub>2</sub>. Overall, the desorption energy values remain fairly consistent, ranging from 0.12 to 0.23 eV. For Na, the desorption energy varies slightly but stays in the range of 0.13–0.20 eV, exhibiting less fluctuation compared to Li. For K, the desorption energy is initially high at 0.67 eV for 1 H<sub>2</sub>, but it drops significantly to a range of 0.11–0.19 eV once 2 H<sub>2</sub> molecules are adsorbed. K exhibits a much higher desorption energy for the first hydrogen molecule (0.67 eV) compared to Li and Na, indicating a stronger initial interaction between K and H<sub>2</sub>, which makes desorption more challenging. In contrast, lithium consistently shows lower desorption energies, suggesting that hydrogen adsorbed on Li can be released more easily than on Na or K. It is observed that *E*<sub>des</sub>(K) > *E*<sub>des</sub>(Na) > *E*<sub>des</sub>(Li) irrespective of the adsorbing atom. The values presented for Li and Na align with the optimal range for effective hydrogen storage, while K may present challenges owing to its initially high desorption energy.

### 3.5 Hydrogen storage capacity and desorption temperature for AM-decorated Bi<sub>2</sub>Se<sub>3</sub>

Hydrogen molecules are progressively bonded to the Li/Na/K–Bi<sub>2</sub>Se<sub>3</sub> compound (Fig. 4). Table 2 analyzes the average energy of hydrogen adsorption evaluated using GGA-PBE.

Nevertheless, the outcomes of both methods exhibit strong agreement. The spatial proximity of H<sub>2</sub> molecules leads to mutual repulsion, yielding a decrease in energy associated with the adsorption of H<sub>2</sub> molecules during the adsorption process. As hydrogen molecules are adsorbed individually, each encounters a slightly distinct environment. Consequently, the adsorption energy of hydrogen on the material's surface may fluctuate slightly. Nonetheless, as the number of hydrogen molecules increases, the difference in adsorption energy between the upper surfaces gradually decreases. Simultaneously, the average separation between H<sub>2</sub> and Bi<sub>2</sub>Se<sub>3</sub> tends to enlarge as adsorption weakens. Initially, polarization induces electrostatic interaction, thereby enhancing adsorption energy. However, as ionized hydrogen molecules gather near lithium atoms, they repel each other owing to electrostatic forces, leading to a reduction in adsorption capacity, particularly as the number of H<sub>2</sub> molecules increases. In essence, polarization reinforces hydrogen molecule adsorption, as electrostatic interactions leading to repulsion between hydrogen molecules reduce subsequent adsorption effectiveness. These opposing phenomena significantly influence hydrogen adsorption.

The maximum hydrogen storage capacity depends on the polarized state and charge repulsion with ongoing molecular hydrogen adsorption onto the surface of Li/Na/K–Bi<sub>2</sub>Se<sub>3</sub>, with adsorption energies of −0.19 eV, −0.19 eV, and −0.18 eV, respectively. The 15th H<sub>2</sub> molecule's bond length is 0.75 Å, which is approximately that of free hydrogen. Eqn (4) is used to determine the gravimetric density of hydrogen. The substrate contains three active sites. The average adsorption energy decreased with increasing hydrogen quantity, with each molecule maintaining a stable adsorption state. Li/Na/K–Bi<sub>2</sub>Se<sub>3</sub> surpasses the DOE's 2025 hydrogen storage goal, fully utilizing the active sites and offering exceptional gravimetric hydrogen density compared to other materials (see Table 4).

Kaur *et al.* explored the capability of alkali metals (two-dimensional carbon–nitride (C<sub>9</sub>N<sub>4</sub>)) functionalized with Li/Na/K monolayers for hydrogen preservation through a primary approach using DFT analyses. The connection between Li/Na/K dopants, such as C<sub>9</sub>N<sub>4</sub>, is strong owing to the charge transfer





from metals to the carbon–nitride monolayer. It was observed that every Li atom in Li@C<sub>9</sub>N<sub>4</sub> can persistently bind as many as 6 H<sub>2</sub> particles without causing structural breakdown, leading to an average adsorption energy of 0.20 eV and remarkably significant hydrogen capacity of 11.9 wt%. Similarly, the storage capacities and average adsorption energies for H<sub>2</sub> for Na- and K-decorated C<sub>9</sub>N<sub>4</sub> complexes are 8.7 wt% and 8.1 wt% with adsorption energy at −0.19 eV and −0.17 eV, respectively, complying with U.S. DOE criteria<sup>65</sup>.

Bi *et al.* investigated the storage efficiency for H<sub>2</sub> in penta-octa-graphene (POG) decorated with low-density alkali metals (Li, Na, and K) using density functional theory. They concluded that 3, 5, and 5 hydrogen molecules involved in polarization and hybridization mechanisms can be consistently adsorbed around each metal atom. POG modified with Li, Na, and K metals shows average H<sub>2</sub> adsorption energy values of −0.15 eV, −0.16 eV, and −0.22 eV, respectively. Binding energies for Li-, Na-, and K-based POG are 2.42, 2.45, and 2.80 eV, respectively, which exceed the cohesive energy. Hydrogen gravimetric densities for Li-, Na-, and K-functionalized POG can attain H<sub>2</sub> storage levels associated with 9.9 wt%, 7.7 wt% and 6.8 wt% in that order, respectively.<sup>69</sup>

L. *et al.* conducted DFT research regarding hydrogen storage in alkali metallic element-decorated tin carbide monolayers (2DSnC), including Li, Na, and K elements. The optimal adsorption location for these alkali metal atoms on 2DSnC is positioned over a tin atom. The data indicate that alkali metal atoms are chemically linked with 2DSnC, with voltage transferring from decorating atoms to 2DSnC. In every case examined, hydrogen molecules were physisorbed onto 2D SnC complexes involving AM, suggesting that these systems may be ideal for storing hydrogen. Specifically, the K-2DSnC single layer demonstrates the most efficient hydrogen storage, with a lone K atom capable of adsorbing as many as 6 hydrogen molecules. Next is Na-decorated 2DSnC, which can uptake 5 hydrogen molecules, followed by Li-decorated 2DSnC, which can adsorb 3 hydrogen molecules. Hydrogen molecule adsorption energies for alkali metal atom-functionalized 2D SnC are −0.20, −0.19, and −0.18 eV. It is likely that when coverage AM concentrations reach 40%, 44%, and 70%, respectively, AM-2D SnC's gravimetric capacities for hydrogen storage could exceed the 5.5 wt% objectives set by US-DOE for automotive technologies.<sup>70</sup>

Halder *et al.* present an in-depth examination of H<sub>2</sub> holding capabilities among alkali metal-functionalized and error-rich 2D boron sheets *via* DFT. The binding energy values for one H<sub>2</sub> molecule on Li- and Na-modified borophene were measured at −0.36 and −0.34 eV per H<sub>2</sub> molecule, respectively. To better understand the H<sub>2</sub> adsorption process and pinpoint electron transfer sources, fluctuations in charge densities and the projected density of states were determined through calculations. The results showed a notable buildup and reduction, leading to intense polarization effects in hydrogen molecules. Ultimately, Na and borophene functionalized with Li achieved weight percent densities of 9.0% and 6.8%, respectively.<sup>71</sup>

### 3.6 Hydrogen desorption temperature ( $T_D$ )

We computed the van't Hoff desorption temperature to determine the feasible desorption temperature using eqn (3) in computational detail,<sup>59,66</sup> with pressure values ranging from 1 to 10 atm. The maximum and minimum desorption temperatures are referenced as  $T_{Dmax}$  and  $T_{Dmin}$ , respectively. These values are designed by considering the uppermost and lowermost adsorption energies. To establish a suitable desorption temperature, we take the estimated normal van't Hoff temperature for desorption ( $T_{Dve}$ ) by averaging  $T_{Dmax}$  and  $T_{Dmin}$ . Supplementary Information 1 presents the maximum, minimum, and average desorption temperatures across the specified pressure range. The  $T_{Dmin}$  for hydrogen desorption in Li/Na/K–Bi<sub>2</sub>Se<sub>3</sub> calculation yields 255.4 K at 1 atm pressure, while the corresponding  $T_{Dmax}$  values at pressure are 676.8 K, 613 K, and 855.6 K, respectively. This indicates that the minimum temperature for Li/Na/K–Bi<sub>2</sub>Se<sub>3</sub> to initiate desorption is 255.4 K under standard conditions, which can be enhanced to 676.8 K, 613 K, and 855.6 K. As pressure increases, the desorption temperature also increases. Fig. 6 shows that Li-/Na-/K-decorated Bi<sub>2</sub>Se<sub>3</sub> can withstand temperatures of up to 906.9 K, 821.3 K, and 1112.2 K at 10 atm. The  $T_{Dve}$  falls within an operational range of 344.8–419.1 K for Bi<sub>2</sub>Se<sub>3</sub>–Li, 319.2–388 K for Bi<sub>2</sub>Se<sub>3</sub>–Na, 408.6–496.7 K for Bi<sub>2</sub>Se<sub>3</sub>–K below a pressure range of 1–5 atm. Analysis of van't Hoff temperature results reinforces the assertion of the reversible hydrogen storage within the operable thermodynamic range of Li/Na/K–Bi<sub>2</sub>Se<sub>3</sub>.<sup>68</sup>

### 3.7 Electronic properties of the Li/Na/K with multiple hydrogens

First, the electronic properties of the PDOS diagrams depicted in Fig. 5(a) demonstrate the 1s orbital of the initially adsorbed hydrogen peaks at −7.62 eV. Although the PDOS diagrams for Bi<sub>2</sub> and Se<sub>3</sub> exhibit minimal variation, there is a notable change in that of lithium. At this energy level, a resonance peak occurs between lithium's 2s and 2p orbitals and hydrogen's 1s orbital, suggesting the relatively weak hybridization of orbital interaction. The lithium 2s atomic orbital experiences hybridization owing to the interplay between lithium and hydrogen, while hybridization of the lithium 2p orbital occurs because, at this juncture, lithium serves as a conduit for the passage of electric charges. As presented in Fig. 5(c), after the adsorption of eighteen molecules of hydrogen, both hydrogen molecules absorb electrons, while the charge on the lithium atom increases rather than decreases. Upon adsorption of eighteen hydrogen molecules, the energy level of the hydrogen 1s orbital broadens and separates beneath the Fermi level. Peaks of s-orbitals disperse into two smaller peaks, suggesting the potential for the adsorption of several hydrogen molecules. Simultaneously, the focal peak of hydrogen 1 orbital shifts toward the left, indicating a transition. The stability of the all-hydrogen molecule's adsorption is inferior to that of the other. In the PDOS of the adsorbed hydrogen material, orbital overlaps between the hydrogen 1s orbital and lithium 2s and 2p orbitals are observed in energies of −7.9, −5.9, and −6.9 eV, indicating electrostatic interaction. This overlap validates the robust bonding between



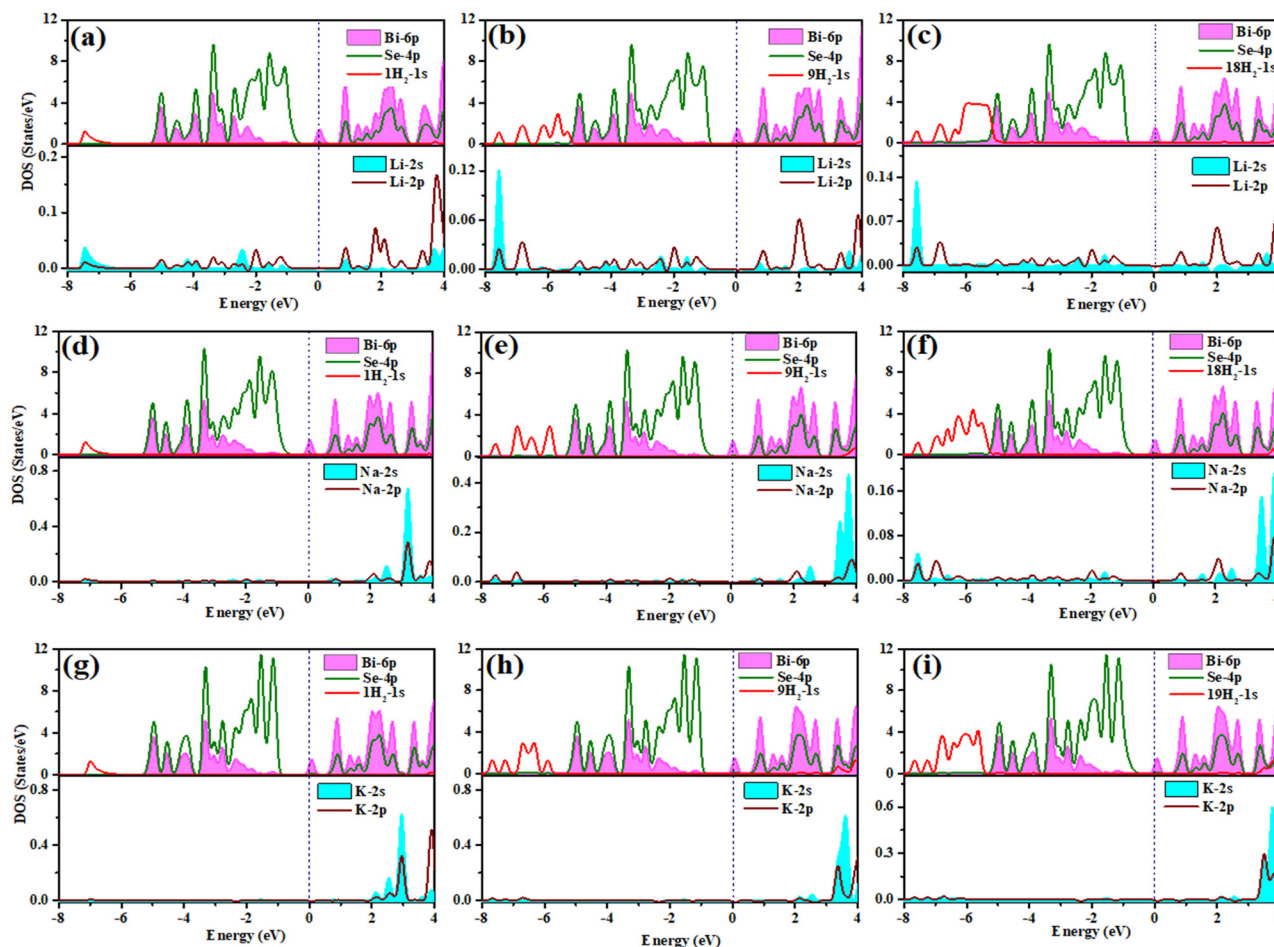


Fig. 5 Projected density of states (PDOS) for (a)  $\text{Bi}_2\text{Se}_3\text{-Li-1H}_2$ , (b)  $\text{Bi}_2\text{Se}_3\text{-Li-9H}_2$ , (c)  $\text{Bi}_2\text{Se}_3\text{-Li-18H}_2$ , (d)  $\text{Bi}_2\text{Se}_3\text{-Na-1H}_2$ , (e)  $\text{Bi}_2\text{Se}_3\text{-Na-9H}_2$ , (f)  $\text{Bi}_2\text{Se}_3\text{-Na-18H}_2$ , (g)  $\text{Bi}_2\text{Se}_3\text{-K-1H}_2$ , (h)  $\text{Bi}_2\text{Se}_3\text{-K-9H}_2$ , and (i)  $\text{Bi}_2\text{Se}_3\text{-K-19H}_2$ .

lithium atoms and hydrogen molecules. This leads to the formation of bonding orbitals of lithium and hydrogen. Charge distribution within hydrogen molecules is split into two segments: an individual hydrogen atom carries an excess of negative charge, while an alternate hydrogen atom shows an excess of positive charge. This evident charge polarization signifies the polarization of the hydrogen molecule.

As depicted in Fig. 5(d), the PDOS diagrams show the initial 1s orbital peak of adsorbed hydrogen at  $-7$  eV. Although the PDOS diagrams for  $\text{Bi}_2$  and  $\text{Se}_3$  remain stable, sodium exhibits a notable change. At this energy level indicated by a resonance peak, weak orbital hybridization occurs between the 2s and 2p orbitals of Na and the 1s orbital of hydrogen. The Na 2s orbital hybridizes owing to its interaction with hydrogen, while its 2p orbital acts as a charge conduit. In  $\text{Na-Bi}_2\text{Se}_3$ , the charge is channeled back to the Na atom, increasing its electron count and confirming the charge transfer.

Hydrogen 1 orbital energy level extends and fragments under the Fermi level, suggesting potential for multiple hydrogen molecule adsorption. Additionally, the maximum of the hydrogen 1s orbital shifts leftward. The stability of adsorbing all hydrogen molecules is lower than that of individual

molecules. In the PDOS of the adsorbed  $\text{H}_2$  material, orbital overlaps are observed between the hydrogen 1s orbital and the Na 2s and 2p orbitals at  $-7.1$ ,  $-6$ , and  $-5.9$  eV, suggesting electrostatic interaction. This overlap indicates strong hybridization between Na atoms and  $\text{H}_2$  molecules, resulting in sodium-hydrogen bond orbitals, where the adsorption process involves local electric field polarization by positive charges and orbital hybridization. This results in the division of charge within the hydrogen molecule, with one atom becoming negatively charged and the other positively charged, indicating polarization.

Fig. 5(g) PDOS presents the initial adsorbed hydrogen's 1s orbital peaks at  $-6.9$  eV. Although  $\text{Bi}_2$  and  $\text{Se}_3$  show little change, there is a significant shift in K-PDOS. A resonance peak appears between the 2s and 2p orbitals of potassium and the 1s orbital of hydrogen, indicating weak orbital hybridization. Potassium's 2s orbital hybridizes owing to hydrogen interaction, while its 2p orbital acts as a charge conduit.  $\text{K-Bi}_2\text{Se}_3$  redirects some charge back to potassium, increasing its electron count and confirming charge transfer. The 1s orbital of hydrogen extends and drops below the Fermi level, suggesting the potential for the adsorption of multiple hydrogen molecules. In the PDOS of adsorbed  $\text{H}_2$  material at  $-7$ ,



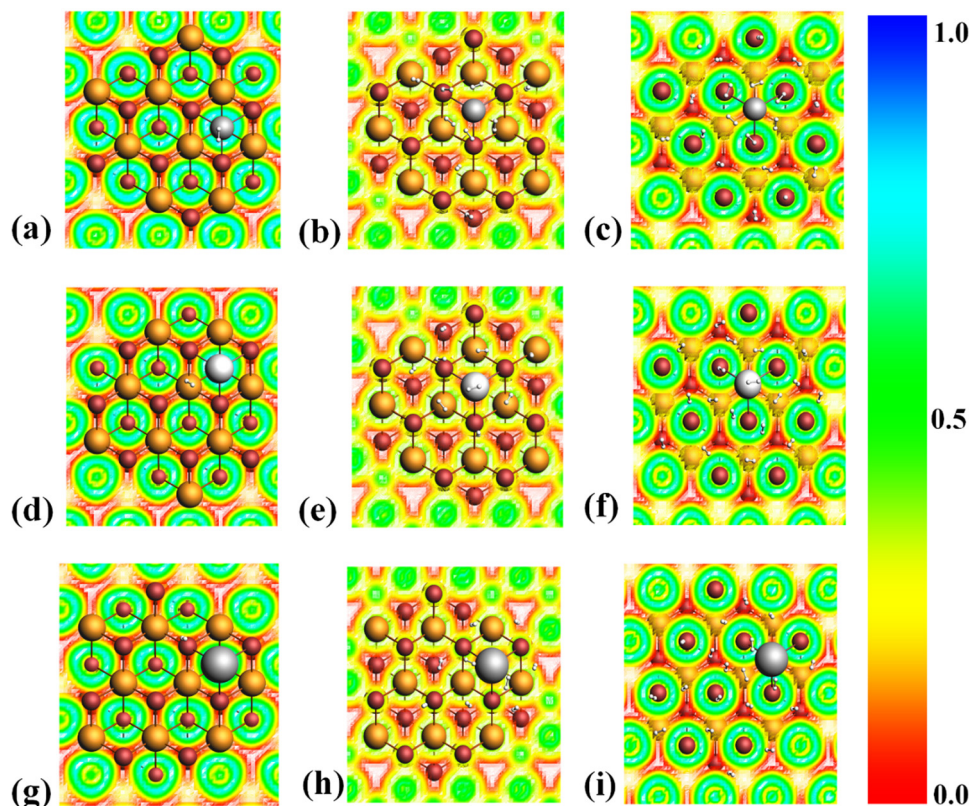


Fig. 6 ELF (a) 1H<sub>2</sub>, (b) 9H<sub>2</sub>, and (c) 18H<sub>2</sub> represent Li-decorated Bi<sub>2</sub>Se<sub>3</sub>; (d) 1H<sub>2</sub>, (e) 9H<sub>2</sub>, and (f) 18H<sub>2</sub> correspond to Na-decorated Bi<sub>2</sub>Se<sub>3</sub>; and (g) 1H<sub>2</sub>, (h) 9H<sub>2</sub>, and (i) 19H<sub>2</sub> represent K-decorated Bi<sub>2</sub>Se<sub>3</sub>.

−6.6, and −5.9 eV, orbital overlaps occur between hydrogen's 1s orbital and K 2s and 2p orbitals, suggesting electrostatic interaction. This overlap confirms robust hybridization between potassium atoms and hydrogen molecules, forming potassium–hydrogen bond orbitals. The bonding process between the substance and hydrogen primarily entails the polarization of positive charges and orbital fusion. The charge

distribution within the hydrogen molecule divides into dual segments: one hydrogen atom carries an excess negative charge, and additional hydrogen holds an excess positive charge, illustrating the molecule's polarization.

### 3.8 Electron localization function

ELF determines the kinetic energy density, which is used to assess electron localization and delocalization. It spans from 0.5 to 1.0, indicating localized electron positions for bonding and nonbonding scenarios. Electron localization typically occurs within nucleus shells, covalent bonds, or lone pairs. Values between 0.0 and 0.5 indicate weak intermolecular van der Waals forces and suggest that electron delocalization manifests across electron shells.

As illustrated in Fig. 6(a), (d), and (g), the prominent green color signifies a decrease in surface charge, with ELF values ranging from 0.5 to 0.0, indicating ionic bonding. Conversely, Fig. 6(b), (e), and (h) depict ELF values between 1.0 and 0.5, suggesting the presence of covalent bonding. Fig. 6(c), (f) and (i) illustrate ELF values between 0.5 and 0.0, indicating ionic bonding.

### 3.9 Hirshfeld charge analysis

Hirshfeld charges are a method for measuring the distribution of atomic charges within a molecule. They are determined from the Hirshfeld surface, which partitions the molecular space

Table 5 Charge transfer of Bi<sub>2</sub>Se<sub>3</sub> on alkali metal Li/Na/K with multiple hydrogen

No. of H <sub>2</sub> molecules	$Q_{\text{Li}}$ (e)	$Q_{\text{Na}}$ (e)	$Q_{\text{K}}$ (e)
1H <sub>2</sub>	0.315	0.480	0.551
2H <sub>2</sub>	0.310	0.465	0.529
3H <sub>2</sub>	0.311	0.454	0.500
4H <sub>2</sub>	0.279	0.723	0.476
5H <sub>2</sub>	0.199	0.407	0.452
6H <sub>2</sub>	0.281	0.375	0.444
7H <sub>2</sub>	0.208	0.374	0.41
8H <sub>2</sub>	0.210	0.357	0.404
9H <sub>2</sub>	0.208	0.315	0.385
10H <sub>2</sub>	0.185	0.292	0.344
11H <sub>2</sub>	0.181	0.267	0.311
12H <sub>2</sub>	0.169	0.197	0.275
13H <sub>2</sub>	0.167	0.218	0.261
14H <sub>2</sub>	0.146	0.178	0.052
15H <sub>2</sub>	0.029	0.047	0.023
16H <sub>2</sub>	0.131	0.184	0.024
17H <sub>2</sub>	0.008	0.211	0.270
18H <sub>2</sub>	0.008	0.174	0.237
19H <sub>2</sub>	—	—	0.241





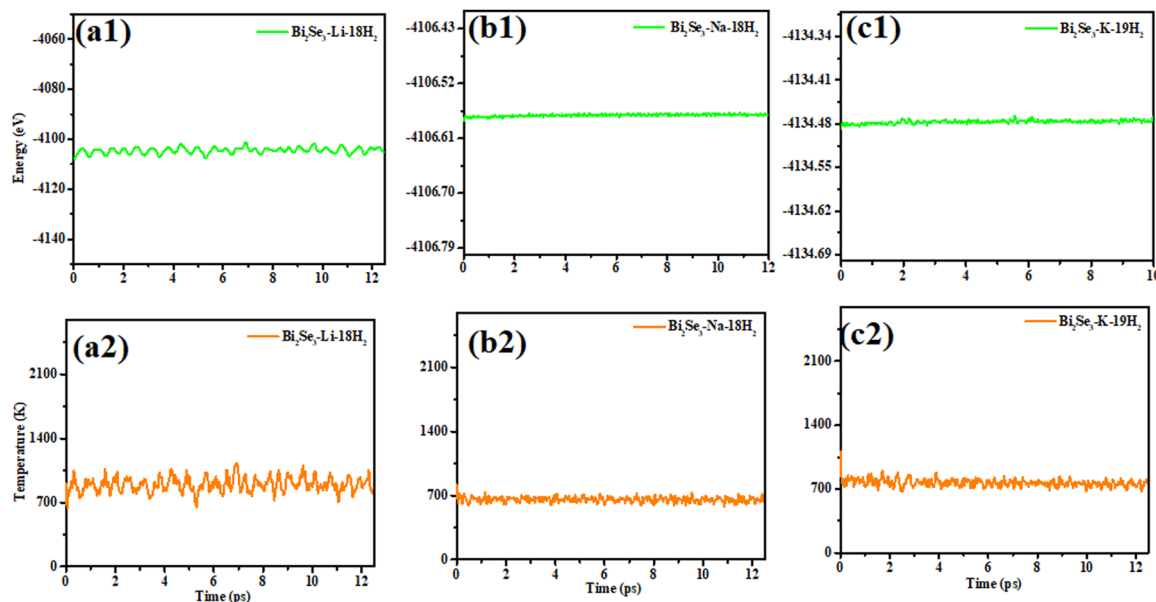


Fig. 7 MD simulation visualizations for the 18H<sub>2</sub>, 18H<sub>2</sub>, and 19H<sub>2</sub> + Li/Na/K–Bi<sub>2</sub>Se<sub>3</sub> systems at 906 K, 821 K, and 1112 K. The outcomes demonstrate the changes in total energy (a1)–(c1) and temperature (a2)–(c2) over time (ps).

into areas around each atom. These charges provide information about the electron density around each atom, indicating whether it is relatively positive or negative. Unlike formal charges, which are fixed, Hirshfeld charges are variable and respond to changes in the molecular environment or structure. They are frequently utilized in computational chemistry to assess molecular characteristics, intermolecular interactions, and chemical reactivity.

The investigation seeks to verify the occurrence of charge transfer between unaltered Bi<sub>2</sub>Se<sub>3</sub> with a shared charge of  $-0.043$  and Bi<sub>2</sub>Se<sub>3</sub> modified with transition metals such as Li, Na, and K. This analysis aims to determine whether these transition metals can transfer charges to the Se sites of the Bi<sub>2</sub>Se<sub>3</sub> layer, with charge values of  $0.315e$ ,  $0.479e$ , and  $0.559e$ , respectively. According to Hirshfeld charge analysis, Bi<sub>2</sub>Se<sub>3</sub> modified with Li and multiple hydrogen atoms shows a high charge transfer on the first hydrogen atom at  $0.315e$ , as shown in Table 5. As the number of hydrogen atoms increases, the charge transfer decreases, with the 18th hydrogen atom having a charge transfer of  $0.008e$ . This indicates that the hydrogen molecules were polarized under the electric field created by the ionized lithium atom. For Na-modified Bi<sub>2</sub>Se<sub>3</sub> with hydrogen adsorption, the charge transfer on the first hydrogen atom is high at  $0.480e$ . However, as the number of hydrogen atoms increases, the charge transfer decreases, with the 18th hydrogen atom showing a charge transfer of  $0.174e$ . Similarly, for K-modified Bi<sub>2</sub>Se<sub>3</sub>, as detailed in Table 5, the charge transfer on 1st hydrogen atom is  $0.551e$ . As the number of hydrogen atoms increases, the charge transfer gradually decreases, with the 19th hydrogen atom showing a charge transfer of  $0.241e$ . Polarization was also confirmed through differential charge analysis, which revealed clear charge accumulation between the hydrogen and Li/Na/K atoms, as well as charge depletion between the hydrogen atoms.

### 3.10 Molecular dynamics simulations

The molecular dynamics (MD) simulations depicted in the figure examine the hydrogen desorption behavior of alkali metal-decorated Bi<sub>2</sub>Se<sub>3</sub> (Li, Na, and K) at different desorption temperatures, and all the simulations were conducted under a constant pressure of 10 atm.<sup>72</sup> The energy evolution of Bi<sub>2</sub>Se<sub>3</sub> systems decorated with Li, Na, and K under hydrogen loading is shown in Fig. 7(a1)–(c1) over a 12-picosecond simulation period. The temperature stability for each system is depicted in Fig. 7(a2)–(c2), where Li-decorated Bi<sub>2</sub>Se<sub>3</sub> stabilizes at a desorption temperature of 906 K, Na-decorated Bi<sub>2</sub>Se<sub>3</sub> stabilizes at 821 K, and K-decorated Bi<sub>2</sub>Se<sub>3</sub> exhibits a higher desorption temperature of 1112 K.

The Li-decorated system (a1) in the energy profiles shows more pronounced fluctuations, indicating dynamic interactions between the hydrogen and the substrate. However, the Na-decorated (b1) and K-decorated (c1) systems exhibit more stable energy behavior, particularly the K-decorated Bi<sub>2</sub>Se<sub>3</sub>, which displays minimal fluctuations but a slightly upward trend. This suggests that K forms stronger binding interactions with hydrogen, leading to higher desorption energy and more difficult hydrogen release than Li and Na.

The simulations indicate that K-decorated Bi<sub>2</sub>Se<sub>3</sub> has the highest desorption temperature (1112 K), demonstrating the strongest interaction with hydrogen, which aligns with K's lower ionization energy than Li and Na. In contrast, Na and Li demonstrate lower desorption temperatures, making them more suitable for applications in which moderate hydrogen release conditions are needed.

AIMD calculations are conducted to investigate the reliability of different configurations. NVT (constant atomic number N, volume V, and temperature T) thermostat remains utilized to sustain a temperature of 400 K during the dynamic simulation,





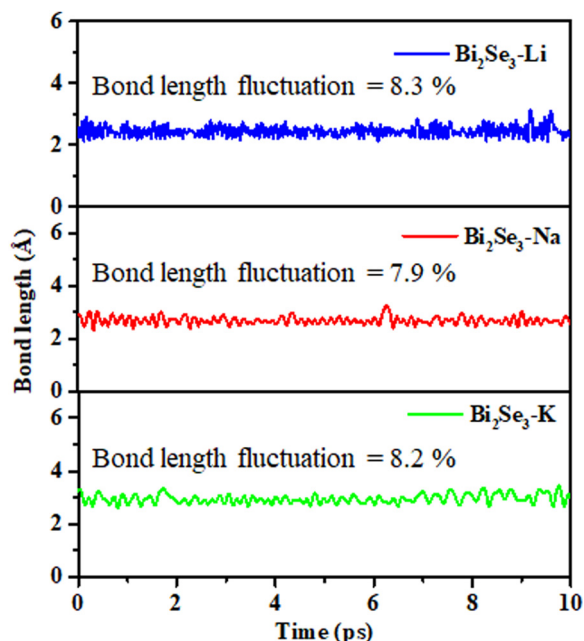


Fig. 8 Fluctuation in the bond length of Li/Na/K atoms in Li/Na/K-Bi<sub>2</sub>Se<sub>3</sub> at 400 K.

utilizing the Andersen thermostat method. In this investigation, the total simulation time was 10 picoseconds, with a time step of 0.25 picoseconds. Fig. 7 illustrates the stability of the Li/Na/K-Bi<sub>2</sub>Se<sub>3</sub> system at 400 K following the AIMD simulation. As shown in Fig. 8, the maximum bond length for lithium adsorption is 3.15 Å at 9 ps, with overall peaks varying between 2.1 and 3.0 Å. For sodium, the maximum bond length is 3.2 Å at 6.2 ps, with the overall peaks between 2.6 and 3.0 Å. In the case of potassium adsorption, the maximum bond length is 3.4 Å at 9.8 ps, while the overall peaks range from 2.7 to 3.3. The small change in total energy implies the absence of unstable weak bonds in these systems.

As a precise indicator of stability, a change in bond length fluctuation of Li/Na/K-decorated Bi<sub>2</sub>Se<sub>3</sub> is observed. During the MD simulations, the bond length fluctuations for Li-Bi<sub>2</sub>Se<sub>3</sub>,

Na-Bi<sub>2</sub>Se<sub>3</sub>, and K-Bi<sub>2</sub>Se<sub>3</sub> throughout 10 picoseconds were plotted at an equilibrium temperature of 400 K. From this plot, it can be concluded that the overall bond length fluctuations for these are 8.3%, 7.9%, and 8.2%, respectively.<sup>73</sup>

### 3.11 Thermodynamic stability analysis

The thermodynamic stability of a hydrogen-adsorbed composite under specific temperature and pressure conditions can be evaluated by calculating its relative energy using the following equation:<sup>17,74</sup>

$$E_r = E_{(\text{Bi}_2\text{Se}_3 + \text{metal} + n\text{H}_2)} - E_{(\text{Bi}_2\text{Se}_3 + \text{metal})} - n[E_{\text{H}_2} - \mu(T, P)], \quad (7)$$

where  $E_{(\text{Bi}_2\text{Se}_3 + \text{metal} + n\text{H}_2)}$ ,  $E_{(\text{Bi}_2\text{Se}_3 + \text{metal})}$ , and  $E_{\text{H}_2}$  are the total energy of the structure, the total energy of the metal-decorated Bi<sub>2</sub>Se<sub>3</sub>, and the energy of the hydrogen, respectively. Here,  $n$  is the number and the  $\mu(T, P)$  can be determined using the following equation:

$$\mu_{\text{H}_2}(T, P) = \Delta H - T\Delta S + k_B T \ln \frac{P}{P_0}, \quad (8)$$

where  $P_0 = 1$  bar and  $k_B$  is the Boltzmann constant. The term  $(\Delta H - T\Delta S)$  represents the change in chemical potential resulting from increasing the temperature from 0 K to the target temperature  $T$  at constant pressure  $P_0$ . In this expression,  $\Delta H$  denotes the change in enthalpy, while  $T\Delta S$  accounts for the entropy contribution. The values of  $(\Delta H - T\Delta S)$  were obtained from the thermochemical NIST database.<sup>75</sup>

Efficient hydrogen storage materials must operate effectively under ambient conditions, particularly near room temperature. To assess this capability, we investigated the thermal stability of the studied systems at their maximum hydrogen storage capacities across a range of temperatures and pressures. Ambient conditions were defined as 298 K and 0.1 MPa for reference.

As shown in Fig. 9(a), the relative energy was plotted as a function of the temperature at standard pressure. A system is considered thermodynamically unstable when relative energy

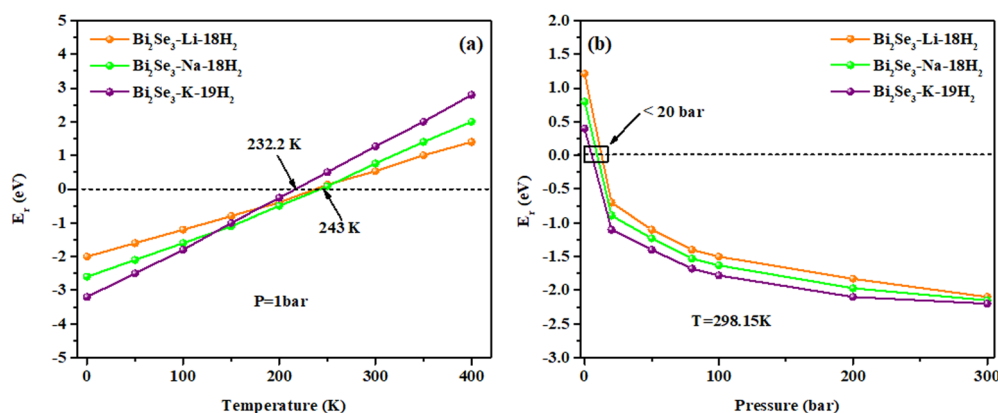


Fig. 9 (a) Temperature-dependent behavior of  $E_r$  for the adsorption of  $n\text{H}_2$  molecules on Li/Na/K-Bi<sub>2</sub>Se<sub>3</sub>-decorated surfaces under standard atmospheric pressure (1 bar). (b) Pressure-dependent variation in  $E_r$  for  $\text{H}_2$  adsorption on Li/Na/K-Bi<sub>2</sub>Se<sub>3</sub>-decorated surfaces at a fixed temperature of 298 K.

becomes positive, signifying the onset of spontaneous hydrogen desorption. The critical temperatures corresponding to this transition are approximately 243 K and 232.2 K for the Li/Na/K-Bi<sub>2</sub>Se<sub>3</sub>-decorated configurations.

Fig. 8(b) presents the variation of relative energy with pressure for the studied systems at room temperature (298 K). Under these conditions, the Bi<sub>2</sub>Se<sub>3</sub> sheets decorated with Li, Na, and K can adsorb up to 18 and 19 hydrogen (H<sub>2</sub>) molecules at pressures below approximately 20 MPa. Notably, hydrogen uptake for all three systems occurs at relatively moderate pressures, demonstrating favorable adsorption behavior under ambient temperature. These pressure requirements closely agree with the operational standards outlined by the U.S. Department of Energy, which indicate that hydrogen refueling stations typically operate within a pressure range of 3–13 MPa, similar to the conditions used for liquefied natural gas (LNG) storage and distribution systems.<sup>76</sup> These results underscore the potential of Li-, Na-, and K-functionalized Bi<sub>2</sub>Se<sub>3</sub> monolayers as promising materials for practical hydrogen storage applications, particularly in onboard fuel cell technologies.

## Conclusions

In summary, the first principles study of alkali metal-decorated Bi<sub>2</sub>Se<sub>3</sub> for hydrogen storage applications has demonstrated the potential of Bi<sub>2</sub>Se<sub>3</sub> as an efficient hydrogen storage material when enhanced with alkali metals, such as Li, Na, and K. The computational analysis revealed significant alterations in the band structure and electronic properties of Bi<sub>2</sub>Se<sub>3</sub> upon decoration with these metals, possibly leading to a metallic nature and improved hydrogen adsorption capabilities. This study showed that Li/Na/K-Bi<sub>2</sub>Se<sub>3</sub> substrates could be achieved within the US DOE criteria. The results indicate that alkali metal-decorated Bi<sub>2</sub>Se<sub>3</sub> is a promising candidate for developing advanced hydrogen storage systems, contributing to broader efforts toward sustainable and efficient energy solutions.

## Conflicts of interest

The authors declare no conflict of interest.

## Data availability

Data are available from the authors upon request.

## Acknowledgements

The authors extend their appreciation to the Deanship of Research and Graduate Studies at King Khalid University, Saudi Arabia, for funding this work through the Large Research Project under grant number RGP-2/712/46.

## References

- 1 M. Wu, M. Gao, S. Qu, Y. Liu, W. Sun, C. Liang, X. Zhang, Z. Li, Y. Yang and H. Pan, LiBH<sub>4</sub> hydrogen storage system with low dehydrogenation temperature and favorable reversibility promoted by metallocene additives, *J. Energy Storage*, 2023, **72**, 108679.
- 2 Q. Hassan, A. Z. Sameen, H. M. Salman, M. Jaszczur and A. K. Al-Jiboory, Hydrogen energy future: Advancements in storage technologies and implications for sustainability, *J. Energy Storage*, 2023, **72**, 108404.
- 3 F. O. Erdogan, C. Celik, A. C. Turkmen, A. E. Sadak and E. Cücü, Hydrogen storage behavior of zeolite/graphene, zeolite/multiwalled carbon nanotube and zeolite/green plum stones-based activated carbon composites, *J. Energy Storage*, 2023, **72**, 108471.
- 4 S.-Y. Lee, J.-H. Lee, Y.-H. Kim, J.-W. Kim, K.-J. Lee and S.-J. Park, Recent progress using solid-state materials for hydrogen storage: a short review, *Processes*, 2022, **10**(2), 304.
- 5 N. Rusman and M. Dahari, A review on the current progress of metal hydrides material for solid-state hydrogen storage applications, *Int. J. Hydrogen Energy*, 2016, **41**(28), 12108–12126.
- 6 E. Boateng and A. Chen, Recent advances in nanomaterial-based solid-state hydrogen storage, *Mater. Today Adv.*, 2020, **6**, 100022.
- 7 M. Simanullang and L. Prost, Nanomaterials for on-board solid-state hydrogen storage applications, *Int. J. Hydrogen Energy*, 2022, **47**(69), 29808–29846.
- 8 Y. Yong, Q. Hou, X. Yuan, H. Cui, X. Li and X. Li, Ultrahigh capacity and reversible hydrogen storage media based on Li-decorated T-BN monolayers, *J. Energy Storage*, 2023, **72**, 108169.
- 9 G. Sanyal, H. T. Nair, P. K. Jha and B. Chakraborty, First principles study on yttrium decorated BeN<sub>4</sub> monolayer for reversible hydrogen storage, *J. Energy Storage*, 2023, **68**, 107892.
- 10 X. Zhang, F. Chen, B. Jia, Z. Guo, J. Hao, S. Gao, G. Wu, L. Gao and P. Lu, A novel lithium decorated N-doped 4, 6, 8-biphenylene for reversible hydrogen storage: Insights from density functional theory, *Int. J. Hydrogen Energy*, 2023, **48**(45), 17216–17229.
- 11 P. Kumar, S. Singh, S. Hashmi and K.-H. Kim, MXenes: Emerging 2D materials for hydrogen storage, *Nano Energy*, 2021, **85**, 105989.
- 12 T. K. N. Pham and J. J. Brown, Hydrogen Sensors Using 2-Dimensional Materials: A Review, *ChemistrySelect*, 2020, **5**(24), 7277–7297.
- 13 M. I. Khan, I. Ashfaq, A. Majid and M. Shakil, Computational designing of Au-decorated buckled bismuthene and its application as a humidity gas sensor, *Mater. Chem. Phys.*, 2023, **295**, 127174.
- 14 M. I. Khan, M. Ashfaq, A. Majid, L. Noor and S. S. Alarfaji, Adsorption of industry affiliated gases on buckled alumene for gas sensing applications, *J. Mol. Model.*, 2023, **29**(8), 267.
- 15 M. I. Khan, S. M. Zaigam, A. Majid and M. B. Tahir, Computational insights of alkali metal (Li/Na/K) atom decorated buckled bismuthene for hydrogen storage, *Int. J. Hydrogen Energy*, 2021, **46**(56), 28700–28708.
- 16 A. S. Shajahan, N. Kalarikkal, N. Garg, Y. Kawazo and B. Chakraborty, A quest to high-capacity hydrogen storage



- in zirconium decorated pentagraphene: DFT perspectives, *Int. J. Hydrogen Energy*, 2022, **47**(85), 36190–36203.
- 17 L. Wang, X. Chen, H. Du, Y. Yuan, H. Qu and M. Zou, First-principles investigation on hydrogen storage performance of Li, Na and K decorated borophene, *Appl. Surf. Sci.*, 2018, **427**, 1030–1037.
  - 18 Y. Zhang, P. Liu, X. Zhu and Z. Liu, A reversible hydrogen storage material of Li-decorated two-dimensional (2D) C<sub>4</sub>N monolayer: First principles calculations, *Int. J. Hydrogen Energy*, 2021, **46**(65), 32936–32948.
  - 19 A. M. Satawara, S. K. Gupta, A. N. Andriotis, M. Menon and P. Gajjar, Capacity development of Pd doped Si<sub>2</sub>BN nanotube for hydrogen storage, *Int. J. Hydrogen Energy*, 2022, **47**(44), 19132–19145.
  - 20 A. M. Satawara, G. A. Shaikh, S. K. Gupta, A. N. Andriotis, M. Menon and P. Gajjar, An ab-initio study of hydrogen storage performance of Si<sub>2</sub>BN nanotubes decorated with group 8B transition metals, *Int. J. Hydrogen Energy*, 2023, **48**(65), 25438–25449.
  - 21 M. R. Mananghaya, Titanium-decorated boron nitride nanotubes for hydrogen storage: a multiscale theoretical investigation, *Nanoscale*, 2019, **11**(34), 16052–16062.
  - 22 S. Yang, H. Yin, G. Lei, Z. Lan, Z. Wang, H. Xu and H. Gu, A DFT study on the promising hydrogen storage performance of a light metal atom-decorated ZnO monolayer, *Int. J. Hydrogen Energy*, 2024, **50**, 71–83.
  - 23 S. Khalid, F. Akhter, A. Saeed, S. S. Alarfaji and M. I. Khan, Exploring hydrogen storage capacity of Sc and Y metal-decorated Molybdenum Tetraboride (MoB<sub>4</sub>) monolayer through DFT calculations, *Phys. Lett. A*, 2025, 130679.
  - 24 J. I. Jason, Y. Pal, P. Anees, H. Lee, T. Kaewmaraya, T. Hussain and P. Panigrahi, Defects induced metallized boron hydride monolayers as high-performance hydrogen storage architecture, *Int. J. Hydrogen Energy*, 2024, **50**, 455–463.
  - 25 Y. Pal, H. Lee, T. Kaewmaraya, K.-F. Aguey-Zinsou, T. Hussain and P. Panigrahi, Enhanced hydrogen storage properties of light metals dispersed boron hydride monolayer, *Int. J. Hydrogen Energy*, 2024, **92**, 1389–1400.
  - 26 V. Mahamiya, J. Dewangan and B. Chakraborty, Interplay between van der Waals, Kubas, and chemisorption process when hydrogen molecules are adsorbed on pristine and Sc-functionalized BeN<sub>4</sub>, *Int. J. Hydrogen Energy*, 2024, **50**, 1302–1316.
  - 27 P. Panigrahi, Y. Pal, H. Lee, K.-F. Aguey-Zinsou and T. Hussain, Efficient and reversible hydrogen storage by light metal-doped BCN monolayers at room temperature, *J. Energy Storage*, 2025, **116**, 115970.
  - 28 K. Alhameedi, A. Karton, D. Jayatilaka and T. Hussain, Metal functionalized inorganic nano-sheets as promising materials for clean energy storage, *Appl. Surf. Sci.*, 2019, **471**, 887–892.
  - 29 Z. Liu, W. Zhao and M. Chai, Li-decorated bilayer borophene as a potential hydrogen storage material: A DFT study, *Int. J. Hydrogen Energy*, 2024, **51**, 229–235.
  - 30 X. Tong, S. Yang, G. Zhu, W. Hou, Q. Wu and J. Li, Lithium doped g-C<sub>6</sub>N<sub>7</sub> monolayer as a reversible hydrogen storage media, *Int. J. Hydrogen Energy*, 2024, **50**, 1477–1488.
  - 31 P. Banerjee, B. Pathak, R. Ahuja and G. Das, First principles design of Li functionalized hydrogenated h-BN nanosheet for hydrogen storage, *Int. J. Hydrogen Energy*, 2016, **41**(32), 14437–14446.
  - 32 R. Rahimi and M. Solimannejad, High-performance hydrogen storage properties of Li-decorated B<sub>2</sub>N<sub>2</sub> nanosheets: a periodic density functional theory study, *Energy Fuels*, 2021, **35**(8), 6858–6867.
  - 33 Y. Yong, S. Hu, X. Yuan, R. Gao, Q. Hou and Y. Kuang, Computational evaluation of Ca-decorated nanoporous CN monolayers as high capacity and reversible hydrogen storage media, *Int. J. Hydrogen Energy*, 2022, **47**(68), 29371–29381.
  - 34 Y.-F. Zhang and J. Guo, Li-decorated 2D Irida-graphene as a potential hydrogen storage material: A dispersion-corrected density functional theory calculations, *Int. J. Hydrogen Energy*, 2024, **50**, 1004–1014.
  - 35 S. Shigetomi and S. Mori, Electrical properties of Bi<sub>2</sub>Te<sub>3</sub>, *J. Phys. Soc. Jpn.*, 1956, **11**(9), 915–919.
  - 36 T. Harman, B. Paris, S. Miller and H. Goering, Preparation and some physical properties of Bi<sub>2</sub>Te<sub>3</sub>, Sb<sub>2</sub>Te<sub>3</sub>, and As<sub>2</sub>Te<sub>3</sub>, *J. Phys. Chem. Solids*, 1957, **2**(3), 181–190.
  - 37 C. Satterthwaite and R. Ure Jr, Electrical and thermal properties of Bi<sub>2</sub>Te<sub>3</sub>, *Phys. Rev.*, 1957, **108**(5), 1164.
  - 38 K. Sujata, P. Patel, P. Gupta and R. G. Solanki, Structural, electronic, and optical properties of orthorhombic and hexagonal phases of Bi<sub>2</sub>Se<sub>3</sub>: First-principles study, *Mater. Today: Proc.*, 2023, 92.
  - 39 S. Augustine, J. Ravi, S. Ampili, T. Rasheed, K. Nair, T. Endo and E. Mathai, Effect of Te doping and electron irradiation on thermal diffusivity of Bi<sub>2</sub>Se<sub>3</sub> thin films by photo-thermal technique, *J. Phys. D: Appl. Phys.*, 2003, **36**(8), 994.
  - 40 A. Marques, D. Miglietta, G. Gaspar, A. Baptista, A. Gaspar, P. Perdigão, I. Soares, C. Bianchi, D. Sousa and B. M. Faustino, Synthesis of thermoelectric magnesium-silicide pastes for 3D printing, electrospinning and low-pressure spray, *Mater. Renew. Sustain. Energy*, 2019, **8**, 1–10.
  - 41 I. Petsagkourakis, K. Tybrandt, X. Crispin, I. Ohkubo, N. Satoh and T. Mori, Thermoelectric materials and applications for energy harvesting power generation, *Sci. Technol. Adv. Mater.*, 2018, **19**(1), 836–862.
  - 42 W. Tian, W. Yu, J. Shi and Y. Wang, The property, preparation and application of topological insulators: a review, *Materials*, 2017, **10**(7), 814.
  - 43 S. Cho, N. P. Butch, J. Paglione and M. S. Fuhrer, Insulating behavior in ultrathin bismuth selenide field effect transistors, *Nano Lett.*, 2011, **11**(5), 1925–1927.
  - 44 D. Kong, W. Dang, J. J. Cha, H. Li, S. Meister, H. Peng, Z. Liu and Y. Cui, Few-layer nanoplates of Bi<sub>2</sub>Se<sub>3</sub> and Bi<sub>2</sub>Te<sub>3</sub> with highly tunable chemical potential, *Nano Lett.*, 2010, **10**(6), 2245–2250.
  - 45 J. Liu, H. Chen, X. Li, H. Wang, Z. Zhang, W. Pan, G. Yuan, C. Yuan, Y. Ren and W. Lei, Ultra-fast and high flexibility near-infrared photodetectors based on Bi<sub>2</sub>Se<sub>3</sub> nanobelts grown via catalyst-free van der Waals epitaxy, *J. Alloys Compd.*, 2020, **818**, 152819.



- 46 J. Buha, R. Gaspari, A. E. Del Rio Castillo, F. Bonaccorso and L. Manna, Thermal stability and anisotropic sublimation of two-dimensional colloidal  $\text{Bi}_2\text{Te}_3$  and  $\text{Bi}_2\text{Se}_3$  nanocrystals, *Nano Lett.*, 2016, **16**(7), 4217–4223.
- 47 Y. Min, G. D. Moon, B. S. Kim, B. Lim, J.-S. Kim, C. Y. Kang and U. Jeong, Quick, controlled synthesis of ultrathin  $\text{Bi}_2\text{Se}_3$  nanodiscs and nanosheets, *J. Am. Chem. Soc.*, 2012, **134**(6), 2872–2875.
- 48 B. Wang, X. Niu, Y. Ouyang, Q. Zhou and J. Wang, Ultrathin semiconducting  $\text{Bi}_2\text{Te}_2\text{S}$  and  $\text{Bi}_2\text{Te}_2\text{Se}$  with high electron mobilities, *J. Phys. Chem. Lett.*, 2018, **9**(3), 487–490.
- 49 Z. Lu, Y. Wu, Y. Xu, C. Ma, Y. Chen, K. Xu, H. Zhang, H. Zhu and Z. Fang, Ultrahigh electron mobility induced by strain engineering in direct semiconductor monolayer  $\text{Bi}_2\text{TeSe}_2$ , *Nanoscale*, 2019, **11**(43), 20620–20629.
- 50 Gt Te Velde, F. M. Bickelhaupt, E. J. Baerends, C. Fonseca Guerra, S. J. van Gisbergen, J. G. Snijders and T. Ziegler, Chemistry with ADF, *J. Comput. Chem.*, 2001, **22**(9), 931–967.
- 51 G. te Velde, F. M. Bickelhaupt, E. J. Baerends, C. Fonseca Guerra, S. J. A. van Gisbergen, J. G. Snijders and T. Ziegler, Chemistry with ADF, *J. Comput. Chem.*, 2001, **22**(9), 931–967.
- 52 J. P. Perdew, K. Burke and M. Ernzerhof, Generalized gradient approximation made simple, *Phys. Rev. Lett.*, 1996, **77**(18), 3865.
- 53 M. Franchini, P. H. T. Philipsen and L. Visscher, The Becke fuzzy cells integration scheme in the Amsterdam Density Functional program suite, *J. Comput. Chem.*, 2013, **34**(21), 1819–1827.
- 54 S. Grimme, Semiempirical GGA-type density functional constructed with a long-range dispersion correction, *J. Comput. Chem.*, 2006, **27**(15), 1787–1799.
- 55 I. Khan Muhammad, K. Swera and M. Abdul, Computational study of 4d transition metals doped bismuthene for spintronics, *Phys. E*, 2021, **126**, 114464.
- 56 E. Anikina, A. Banerjee, V. Beskachko and R. Ahuja, Li-decorated carbyne for hydrogen storage: charge induced polarization and van't Hoff hydrogen desorption temperature, *Sustainable Energy Fuels*, 2020, **4**(2), 691–699.
- 57 Z. Sheng, S. Wu, X. Dai, T. Zhao and Y. Hao, A first-principles study of hydrogen storage capacity based on Li–Na-decorated silicene, *Phys. Chem. Chem. Phys.*, 2018, **20**(20), 13903–13908.
- 58 Y. Ji, H. Dong and Y. Li, Theoretical predictions on Li-decorated borophenes as promising hydrogen storage materials, *ChemistrySelect*, 2017, **2**(31), 10304–10309.
- 59 R. Y. Sathe, H. Bae, H. Lee and T. D. Kumar, Hydrogen storage capacity of low-lying isomer of  $\text{C}_{24}$  functionalized with Ti, *Int. J. Hydrogen Energy*, 2020, **45**(16), 9936–9945.
- 60 B. Chettri, P. Patra, N. N. Hieu and D. Rai, Hexagonal boron nitride (h-BN) nanosheet as a potential hydrogen adsorption material: A density functional theory (DFT) study, *Surf. Interfaces*, 2021, **24**, 101043.
- 61 L.-B. Zhan, C.-L. Yang, M.-S. Wang and X.-G. Ma, Two-dimensional  $\text{Bi}_2\text{Se}_3$  monolayer with high mobility and enhanced optical absorption in the UV-visible light region, *Phys. E*, 2020, **124**, 114272.
- 62 S. Haldar, Hydrogen storage in Li decorated and defective pentaocite phosphorene: A density functional theory study, *Int. J. Hydrogen Energy*, 2023, **48**(21), 7794–7806.
- 63 C. Kittel, *Introduction to solid state physics*, John Wiley & sons, inc., 2005.
- 64 P. Liu, H. Zhang, X. Cheng and Y. Tang, Hydrogen adsorption on Li-decorated BN analogs of  $\gamma$ -graphyne: a DFT study, *Comput. Mater. Sci.*, 2016, **125**, 28–35.
- 65 S. P. Kaur, T. Hussain, T. Kaewmaraya and T. D. Kumar, Reversible hydrogen storage tendency of light-metal (Li/Na/K) decorated carbon nitride ( $\text{C}_9\text{N}_4$ ) monolayer, *Int. J. Hydrogen Energy*, 2023, **48**(67), 26301–26313.
- 66 S. Hu, Y. Yong, Z. Zhao, R. Gao, Q. Zhou and Y. Kuang,  $\text{C}_7\text{N}_6$  monolayer as high capacity and reversible hydrogen storage media: A DFT study, *Int. J. Hydrogen Energy*, 2021, **46**(42), 21994–22003.
- 67 Y. Zhang, L. Zhang, H. Pan, H. Wang and Q. Li, Li-decorated porous hydrogen substituted graphyne: a new member of promising hydrogen storage medium, *Appl. Surf. Sci.*, 2021, **535**, 147683.
- 68 R. Y. Sathe, M. Ussama, H. Bae, H. Lee and T. J. Dhilip Kumar, Density functional theory study of Li-functionalized nanoporous R-graphyne–metal–organic frameworks for reversible hydrogen storage, *ACS Appl. Nano Mater.*, 2021, **4**(4), 3949–3957.
- 69 L. Bi, Z. Miao, Y. Ge, Z. Liu, Y. Xu, J. Yin, X. Huang, Y. Wang and Z. Yang, Density functional theory study on hydrogen storage capacity of metal-embedded penta-octa-graphene, *Int. J. Hydrogen Energy*, 2022, **47**(76), 32552–32564.
- 70 A. L. Marcos-Viquez, A. Miranda, M. Cruz-Irisson and L. A. Pérez, Tin carbide monolayers decorated with alkali metal atoms for hydrogen storage, *Int. J. Hydrogen Energy*, 2022, **47**(97), 41329–41335.
- 71 S. Haldar, S. Mukherjee and C. V. Singh, Hydrogen storage in Li, Na and Ca decorated and defective borophene: a first principles study, *RSC Adv.*, 2018, **8**(37), 20748–20757.
- 72 A. Abbasi and J. Jahanbin Sardroodi, Structural and electronic properties of group-IV tin nanotubes and their effects on the adsorption of  $\text{SO}_2$  molecules: insights from DFT computations, *J. Appl. Phys.*, 2018, **124**(16), 124.
- 73 G. Sanyal, S. Lakshmy, A. Vaidyanathan, N. Kalarikkal and B. Chakraborty, Detection of nitrobenzene in pristine and metal decorated 2D dichalcogenide  $\text{VSe}_2$ : Perspectives from density functional theory, *Surf. Interfaces*, 2022, **29**, 101816.
- 74 B. J. Cid, A. N. Sosa, Á. Miranda, L. A. Pérez, F. Salazar, A. I. Mtz-Enriquez and M. Cruz-Irisson, Enhanced reversible hydrogen storage performance of light metal-decorated boron-doped silicene: A DFT study, *Int. J. Hydrogen Energy*, 2022, **47**(97), 41310–41319.
- 75 M. Chase Jr, J. Curnutt, J. Downey Jr, R. McDonald, A. Syverud and E. Valenzuela, JANAF thermochemical tables, 1982 supplement, *J. Phys. Chem. Ref. Data*, 1982, **11**(3), 695–940.
- 76 A. B. Klass and D. Meinhardt, Transporting oil and gas: US infrastructure challenges, *Iowa L. Rev.*, 2014, **100**, 947.

